First Principles Calculations on Thermodynamic Properties and Magnetism of κ-carbide and Monte-Carlo Cell Gas Model

by

SEO ,Seung-Woo
Computational Metallurgy
Graduate Institute of Ferrous Technology
Pohang University of Science and Technology

A thesis submitted to the faculty of Pohang University of Science and Technology in partial fulfillments of the requirements for the degree of Master of Science in the Graduate Institute of Ferrous Technology (major)

Pohang, Korea
20. 12. 2010
Approved by

Prof. H. K. D. H. Bhadeshia
Major Advisor

First Principles Calculation on Thermodynamic Properties and Magnetism of κ-carbide and Monte Carlo Cell Gas Model

SEO, Seung-Woo

This dissertation is submitted for the degree of Master of Science at the Graduate Institute of Ferrous Technology of Pohang University of Science and Technology. The research reported herein was approved by the committee of Thesis Appraisal

20. 12. 2010

Thesis Review Committee

Chairman:H. K. D. H. Bhadeshia   (signature)

Member: Dong Woo Suh   (signature)

Member: In Gee Kim   (signature)

Member: Se Kyun Kwon   (signature)

First principles calculation on thermodynamic properties and magnetism of κ-carbide and Monte-Carlo cell gas model

Abstract

(Fe,Mn)$_3$AlC κ-carbides are important substance in high strength light-weight steels. κ-carbide is known to initiate crack and propagate the crack or, otherwise, pin the slips and make uniform shear bands. These opposite properties was decided by environment of the system. Therefore phase diagram of Fe-Mn-Al-C quaternary system and κ-carbide is vital for this kind of steels. However, there is no solid thermodynamic value and stability of κ-carbide. To work towards this goal, the all-electron full potential linearized augmented plane-wave method(FLAPW) was used within the generalized gradient approximation. The formation enthalpies of various κ-carbides are calculated. All of κ-carbides have negative formation enthalpy. The lowest κ-carbide formation was Fe$_2$MnAlC which is $9.5\,\mathrm{kJ}\,\mathrm{atom}\text{-}\mathrm{mol}^{-1}$ lower than the highest formation Fe$_3$AlC. When the carbon position was changed to another octahedral position in Fe$_2$MnAlC, the formation energy becomes positive but magnetic moment was increased. In this research, first-principles calculation result was reassessed using Monte-Carlo cell gas model. The result of Monte-Carlo simulation showed smaller entropy value than configurational entropy caused by

implementation problem. However, general temperature dependence of free energy, entropy, specific heat and internal energy is well predicted by simulation. In the future work, we hope to incorporate the calculated energies in to phase diagram calculation methods and modify cell gas model to improve implementation problem.

Contents

Nomenclature

$\bar{d}$ The man size of brittle particle of the particle population respectively

$\hbar$ The reduced Plack's constant, $\hbar = h/2\pi$

$\mathbf{G}_j$ The three dimensional reciprocal lattice vector

$\mathbf{r}_i$ The position vector of electron

μ_{B} The Bohr magneton

Ψ The wave function of the electrons

ρ_{iron} The density of pure state iron

σ The tensile stress acting on the particle

σ_{min} The minimum fracture stress of the particle

A_2 The Curie temperature

A_{CM} The temperature at which austenite transforms to cementite during cooling process.

A_C The critical temperature for heating process

A_{e1} The equilibrium eutectoid reaction temperature

A_{e3} The equilibrium temperature at which α-ferrite transforms to austenite

A_{e4} The equilibrium temperature at which austenite transforms to δ-ferrite

A_e The critical temperature for equilibrium

A_r The critical temperature for cooling process

$C(T)$ The specific heat of the system at temperature T

d The size of brittle particle of the particle population respectively

DOS The density of the states

E The total energy of the system

e The charge of electron

F The Helmholtz free energy

$g(E)$ The density of the states at energy level E

H The hamiltonian of the system

k_{B} The Boltzmann constant

m The Weibull inhomogeneity factor

m_e The mass of electron

$n(\mathbf{r})$ The electronic density function

P_{fr} The possibility of fracture

S The entropy of the system

U The internal energy of the system

u_l The solution of the radial Schrödinger equation solved at a fixed energy parameter E_l

v_{ee} The electron-electron interaction

v_{ext} The external potential by atom

v_{XC} The exchange-correlation potential

Y_{lm} The spherical harmonics at quantum number l and m

Z The partition function for classical system

Fe_2MnAlC (octa-1) The κ-carbide with E2$_1$ structure

Fe_2MnAlC (octa-2) The octahedral carbon position with four Fe atoms and two Al atoms

Fe$_2$MnAlC (octa-3) The octahedral carbon position with two Mn atoms, two Fe atoms, and two Al atoms

Fe$_{3-x}$Mn$_x$AlC The structure with x iron atoms replaced by x Mn atoms

1 Introduction

It is good to be save energy and to protect the environment. Most parts of cars and ships are made of steels, so on way forward is to reduce the density of steel while maintaining the properties such as toughness, which ensure safety.

Light-weight steel design are usually exploit manganese, aluminum, and carbon as alloying elements (Frommeyer and Brüx, 2006; Chin et al., 2010; Chang et al., 2010).

Manganese is a well-known austenite stabilizer and increases strength and hardness of steels. However, large concentration can reduce the ductility and weldability. Carbon also stabilizes austenite and forms various carbides for instance, cementite (Fe_3C) and κ-carbide (Fe_3AlC, Fe_2MnAlC) which has a huge effect on steel properties. Aluminum is the key element in lowering density of steel because it is light element. These Fe-Mn-Al-C quaternary steels have been researched in the contest of transformation induced plasticity (TRIP) steels and twin induced plasticity (TWIP) steels.

Frommeyer and Brüx (2006) reported that uniformly distributed nano-size κ-carbide supported a shear-band induced plasticity (SIP effect). The density of steel was at least $10\,\%$ less than pure iron and the specific energy absorption at a high strain rate of $10^3\,\mathrm{s}^{-1}$ was $0.43\,\mathrm{J\,mm}^{-3}$ which is

		Fuel Economy Benefit (%)					
		Small Car			Mid-size Car		
	Velocity	30 MPH	45 MPH	60 MPH	30 MPH	45 MPH	60 MPH
Weight	5%	3.3	2.6	1.9	3.6	2.4	1.9
Reduction	10%	6.0	4.8	3.5	7.1	4.9	3.8
	20%	12.7	10.0	7.2	15.1	10.1	7.9

Table 1.1: Simulation results of automobile fuel economy with varying weight reduction. A small car has an additional 300 lb with 2 passengers. Mid-sized car has an additional 450 lb with 3 passengers (Casadei and Broda, 2008).

very close to the value of TWIP steel. This κ-carbide also can be found in Fe-Al-C ternary alloys and it has a hardening effect on the system (Pang and Kumar, 1998, 2000). Kimura et al. (2004) showed that the location of κ-carbide has a noteworthy effect on steel strength and elongation. The lattice misfit between κ and austenite (γ) can be controlled by the nickel and aluminum contents (Kimura et al., 2002; Tian et al., 2008), and furthermore, the stacking fault energy can be managed to stimulate the SIP effect when this is $110\,\mathrm{mJ\,m^{-2}}$ (Frommeyer and Brüx, 2006). It is clear that controlling of κ-carbide is important for making this kind of steel. There is

work to figure out thermodynamic and general properties by experiments (Frommeyer and Brüx, 2006; Chang et al., 2010; Pang and Kumar, 1998, 2000; Kimura et al., 2004, 2002; Tian et al., 2008; Palm and Inden, 1995; Choo et al., 1997; Choo and Han, 1985; Ishida et al., 1990; Han et al., 2010), and theory (Chin et al., 2010; Ishida et al., 1990; Connetable et al., 2008; Ohtani et al., 2004; Maugis et al., 2006; Connetable and Maugis, 2008). However these deal only with ternary κ-carbide (Fe_3AlC) and the calculated formation energies are uncertain because it is too method dependent (Table 1.3). There are also experiment results that the magnetism of Fe-Mn-Al-C quaternary system can be changed with κ carbide precipitation (Sato et al., 1990).

In this work, formation enthalpy at $0\,K$ of Fe_3AlC, Fe_2MnAlC, $FeMn_2AlC$, and Mn_3AlC and their magnetic properties were investigated with first-principles calculation, specifically, by using the full-potential linearized augmented wave (FLAPW) method (Wimmer et al., 1981; Weinert et al., 1982) based on the generalized gradient approximation (GGA) implemented in the QMD-FLAPW package. Also, new concept of cell gas Monte-Carlo simulation was designed with calculated total energy of materials without a database.

1.1 Fe-Mn-Al-C High Manganese and High Aluminum Steels

High manganese and high aluminum steels have been expected to replace Fe-Cr-Ni-C stainless steels for its corrosion resistance, light weight, cheap price and good combination of ductility and strength (Frommeyer and Brüx, 2006; Chang et al., 2010). Fe-Mn-Al-C or Fe-Mn-C system steels have three significant deformation modes as a function of stacking-fault energy.

TRIP steel exploits the transformation of austenite to martensite at stress concentration. This transformation has a role of work hardening, homogeneous deformation and decentralization of stress.

TWIP steels get benefit from the mechanical twinning of austenite. The shear strain induced by twinning is $s = 1/\sqrt{2} \approx 0.707$ and that induced by displacive transformations is 0.25. So, the strain obtained by twinning is more than twice that of simple shear.

Normally, TRIP and TWIP steels have much better mechanical properties than SIP steels but, if fine κ-carbides harder dislocation movement, SIP steels can replace the other two. Moreover, SIP steels contain 6 to 12 mass% of aluminum so they are much lighter then TRIP or TWIP steels. For TRIP and TWIP steels, there is a limitation to the aluminum amount because it increases the stacking fault energy and leads to the suppression of TRIP and TWIP.

However, cracking is reported during cold rolling (Han et al., 2010), initi-
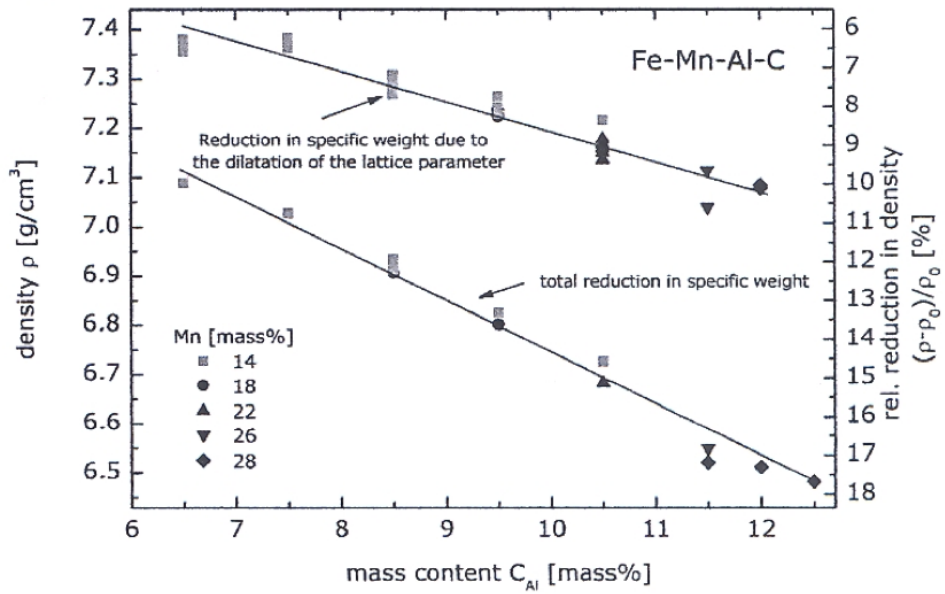
Figure 1.1: Density as function of the aluminum concentration of diverse Fe-xMn-yAl-zC steels with varying manganese contents (14 mass% to 28 mass%). The lower linear curve represents the overall reduction in density with increasing aluminum concentration. The upper curve shows the decrease in density due to the expansion of the γ-lattice. The density of pure iron is $\rho_{iron} = 7.874\,\mathrm{g\,cm^{-3}}$ at room temperature (Frommeyer and Brüx, 2006).

ated from the ferrite and κ-carbide boundaries. The reason of cracking was coarsened κ-carbide and position. So, controlling of κ-carbide precipitation is very important. Kimura et al. (2004) dealt with this effect and reported lamella structure of ferrite and κ-carbide make steel more ductile and can reduce cracking.

1.2 κ-carbide

1.2.1 Formation and Crystal Structure

The formula of κ-carbide is $(Fe,Mn)_3AlC$; aluminum atoms are located on each corner of the cubic unit cell, iron and manganese are placed on the face centers, and carbon is at the center of unit cell (octahedral site made by iron and manganese). The unit cell of κ-carbide is shown in Fig. 1.2. With the *Strukturbericht Designation*, this type of structure is $E2_1$ or called "an anti-perovskite-type" structure.

In the perovskite structure for example, $BaTiO_3$, titanium, which is a transition metal, is located at the center of the unit cell, and oxygen, the non-metallic atom, occupies the face center. However, the face centers of κ-carbide are filled with transition metal and center of the unit cell is occupied by non-metallic carbon atom, so κ-carbide structure is called an "anti-perovskite" sturucture.
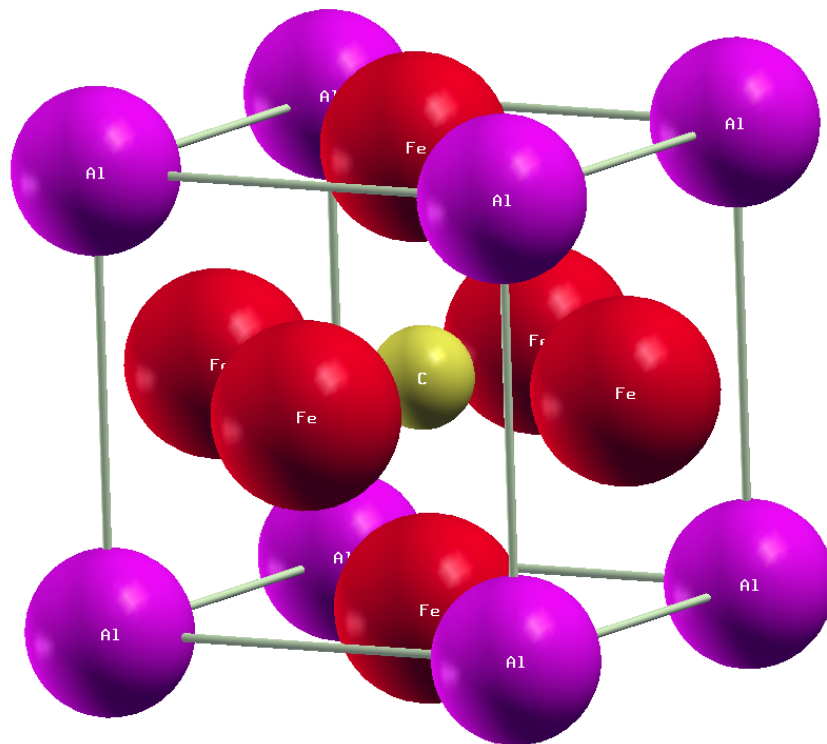
14

Figure 1.2: Unit cell of κ-carbide : aluminum occupies each corner, iron and manganese are located on face centers and the carbon atom is placed at the center of the unit cell which is also an octahedral site made by iron and manganese.

1.2.2 Different Octahedral Site of Fe$_2$MnAlC κ-carbide

There are three different octahedral sites possible in Fe$_2$MnAlC κ-carbide. Fig. 1.3. shows the octahedral sites. Even if there is position exchange between Al, Fe, and Mn atoms, the only difference is apparent for the carbon octahedral site. This property was used for Monte-Carlo simulation as a cell gas model.

In the chapter 4.2, the formation enthalpies of different carbon octahedral sites were also calculated by using first-principles and with the results, a cell-gas model was made to estimate the free energy with Monte-Carlo simulation.

1.2.3 Role of κ-carbide in the Fe-Mn-Al-C and Fe-Al-C System

In general, carbide is harder than pure iron and strengthens steels. However, it can also be brittle, therefore, it initiates cracks or helps the propagation of cracks. Wallin et al. (1986) reported the effect of brittle particles in a ductile matrix on fracture by using a weakest link model, which is

$$P_{fr} = 1 - \exp\left\{-\left(\frac{d}{\bar{d}}\right)^3 \cdot \left(\frac{\bar{d}}{d_N}\right)^3 \cdot \left(\frac{\sigma - \sigma_{min}}{\sigma_0 - \sigma_{min}}\right)^m\right\} \qquad (1.1)$$

where d and $\bar{d}$ are brittle particle and mean size of the particle population respectively, σ is the tensile stress acting on the particle, σ_{min} is the mini-
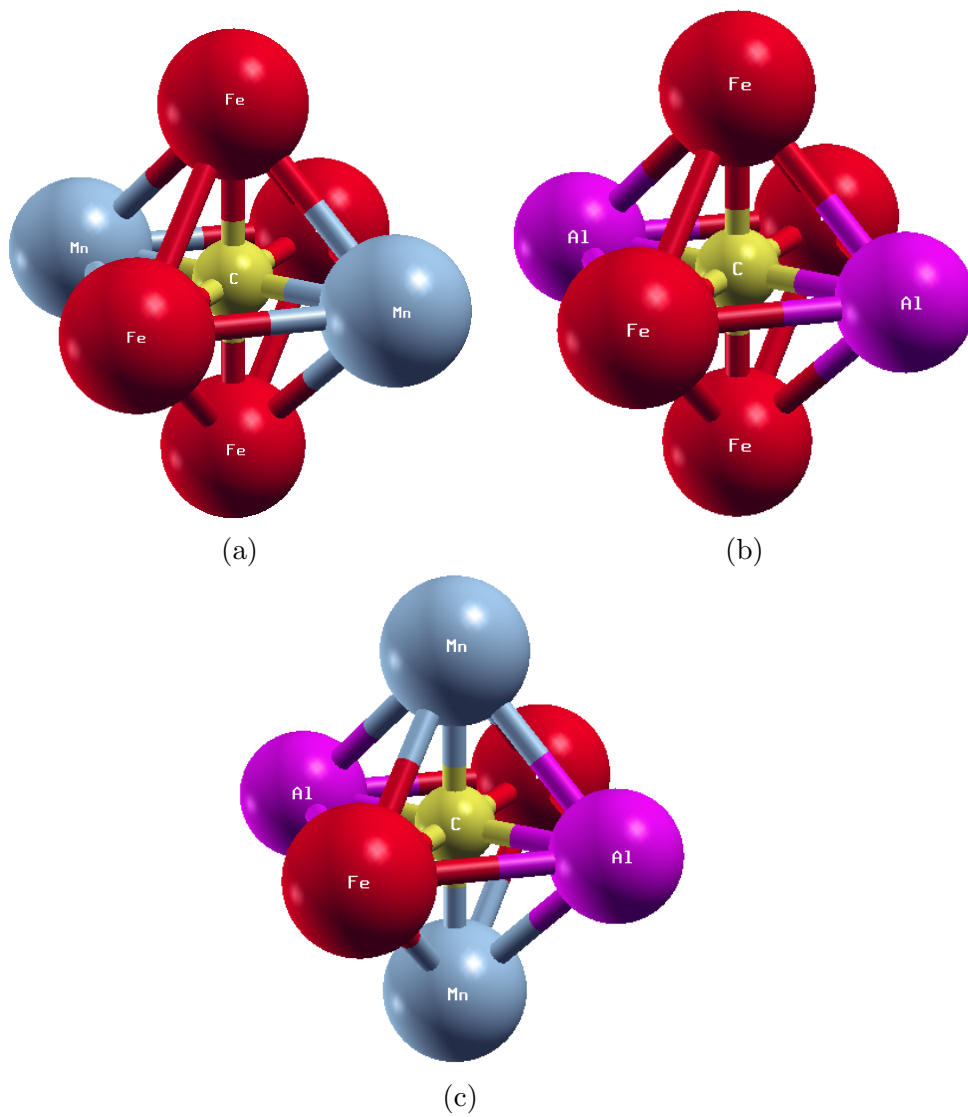
Figure 1.3: Possible configurations for octahedral sites which contain carbon. Octahedral site made by (a) four Fe atoms and two Mn atoms, (b) four Fe atoms and two Al atoms, (c) two Mn atoms, two Fe atoms and two Al atoms.

17

mum fracture stress of the particle, m is Weibull inhomogeneity factor, and σ_0 and d_N are normalizing parameters (Wallin et al., 1986).

According to Eq. 1.1, the probability of fracture is increased when,

1. the size of the brittle particle increases,

2. the brittle particles exist continuously, in which case they can be treated like an one big particle.

Also, the phase which is surrounding κ-carbide is important. For example, coarsened κ-carbide in a phase boundary can easily initiate cracks which propagate (Fig. 1.4) when austenite (γ) coexists with κ (Kimura et al., 2004). Indeed, if there is ferrite, the crack will go through the ferrite (Fig. 1.5) and non-work hardened ferrite in the κ-carbide inhibits crack propagation or changes the direction of crack (Fig. 1.6) (Han et al., 2010). The experiments on fine κ-carbide was reported by Frommeyer and Brüx (2006). In their work, nano-size κ-carbide was regularly distributed and coherent with austenite and it sustained homogeneous shear band acquired by dislocation glide. As a result, ductility is remarkably improved and the specific energy absorption is as high as that of TWIP steels.

Scattered κ-carbide on phase boundaries is usually the initial point of cracks. When austenite coexists with κ-carbide, cracks propagate along κ-carbide or along the boundary between κ and austenite. However, when
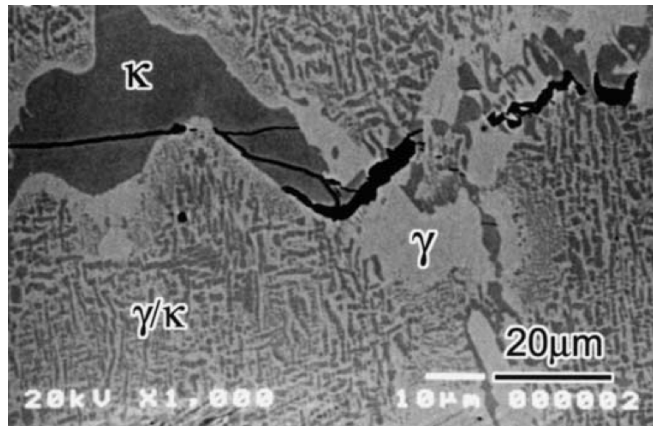
18

Figure 1.4: A back-scattered electron image of the tensile specimen in the vicinity of fracture surface of the Fe-29Mn-9Al-2.6C (in mass%) alloy (Kimura et al., 2004).

κ is in ferrite, the crack rapidly moves into the ferrite. With high manganese and high aluminum contents, austenite is highly stable so phase transformation to ϵ-martensite would not happen and the stacking fault energy is too high to induce mechanical twinning. So shear band induced plasticity will be the primary deformation mode. κ-carbide sustains shear bands so, it is possible for those to be uniformly dispersed. However, to obtain good ductility via the SIP effect, κ-carbide should be fine and coherent with the austenite (Frommeyer and Brüx, 2006). It clearly is necessary to strictly control the precipitation of κ-carbide.
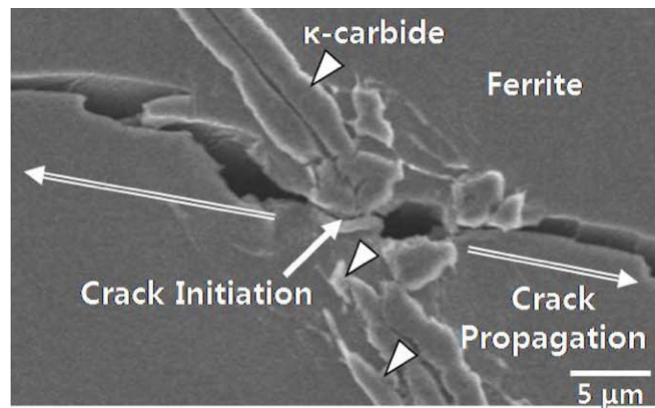
19

Figure 1.5: Scanning Electron Microscope (SEM) micrographs of the cross-sectional area beneath the tensile fracture surface of the Fe-(4 6)Mn-(6 8)Al-0.1C (mass%) alloy. Crack was initiated in κ-carbide and rapidly propagated into ferrite (Han et al., 2010).
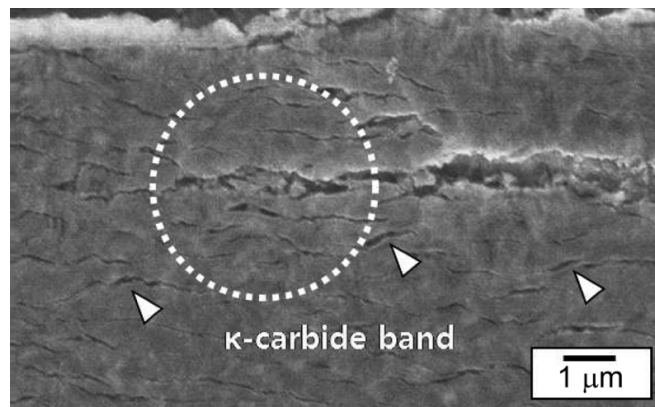

Figure 1.6: SEM micrographs of the cross-sectional area beneath the tensile fracture surface of the Fe-(4 6)Mn-(6 8)Al-0.3C (mass%) alloy. Crack in the κ-carbide band is short and discrete (Han et al., 2010).

1.3 Thermodynamics and Kinetics of κ-carbide and Related Phases

Pure iron is unusual at ambient pressure. At room temperature, the BCC signified by α is the stable form. When the temperature is raised to A_{c3} which is 910 °C, the ferrite transform to FCC austenite denoted by γ. If the temperature reaches to 1390 °C, austenite becomes ferritic again, traditionally denoted by δ even it has same structure as α-ferrite apart from magnetic properties. Alloying with carbon drastically changes the phase fields. So, an important feature in steel research is the phase diagram of Fe-C binary system (Bhadeshia and Honeycombe, 2006). Fig 1.7 shows the iron-iron carbide equilibrium phase diagram.

In Fig 1.7, austenite (γ) has the largest phase field compared with α- and δ-ferrite, reflecting the solubility of carbon in each phase. The maximum solubility of carbon in austenite is about 2 mass%, and 0.025 mass% for α-ferrite.

There are many temperatures and critical points shown in Fig 1.7. First, A_{e1} is the eutectoid reaction temperature at 723 °C. Second, there is the A_{e3} temperature at which austenite becomes the stable phase. For pure iron it is 910 °C but it decreases as the carbon content increases. Third, the δ-ferrite transition temperature of austenite which is called A_{e4} and 1390 °C for pure iron. Carbon addition makes A_{e4} higher. A_2 is the Curie
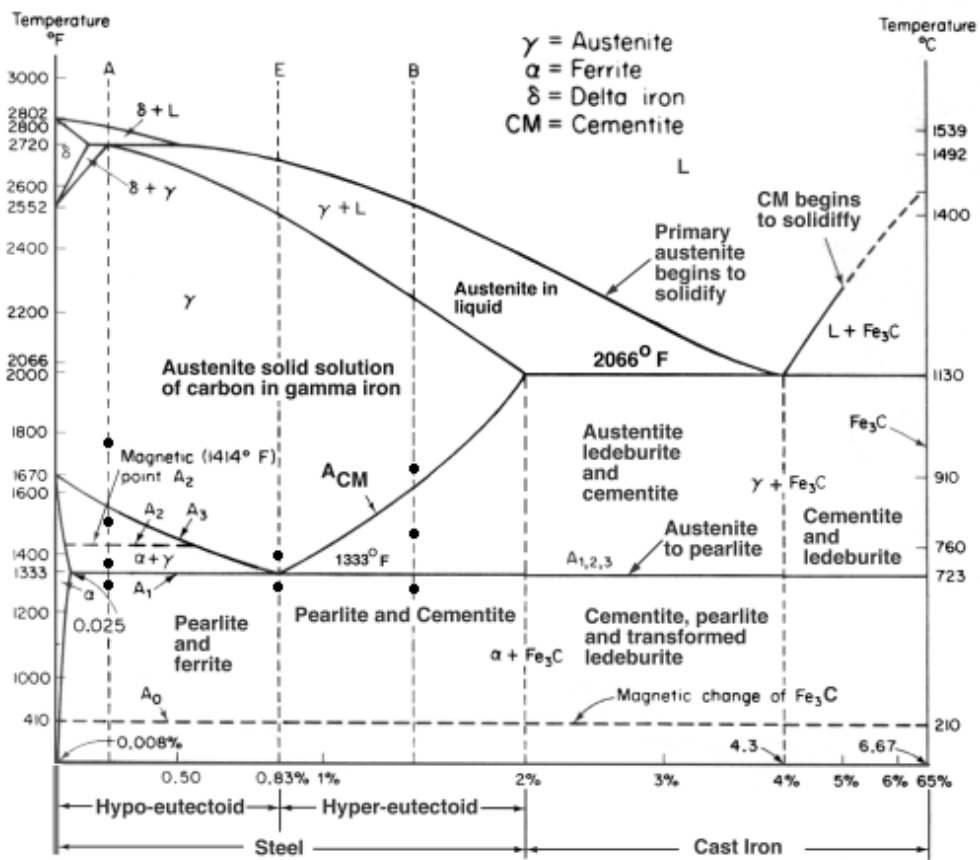
Figure 1.7: The Fe-Fe₃C equilibrium phase diagram (Pollack, 1988).

temperature at which magnetic phase transition happens the from ferro-
to para-magnetic states, independent of the carbon content. The A_{CM}
temperature is that at shich cementite (Fe_3C) is formed an cooling from
austenite. These temperatures can be measured, but there is some hystere-
sis between cooling and heating. So, each temperatures has A_C for heating
(chauffage), A_r for cooling (refroidissement), and A_e (equilibrium). How-
ever, A_C and A_r are sensitive to heating and cooling rate.

There are many alloying elements which are used in steels and their effect
can be classified by their ability to stabilize austenite. Fig 1.8 displays the
four classes of alloying effects.

Fig 1.8a shows the effect of elements which include nickel and manganese
which promote austenite. This type of alloying element can totally remove
α- and δ-ferrite. Therefore, nickel and manganese lower the A_{e4} and A_{e3}
to room temperature and it makes easier to retain austenite.

Fig 1.8b represents the example of alloying elements which expand the γ
field. Carbon is typical element in this class. This type of element usually
makes a compound with iron so expansion of γ-phase field is limited.

Fig 1.8c shows a closed γ-field, due to an element which heavily suppresses
the austenite phase field, and connect the δ- and α-ferrite phase fields. Alu-
minum, silicon, and phosphorus come in this category.

A contracted γ-field is shown in Fig. 1.8 (d). The two forms of ferrite are
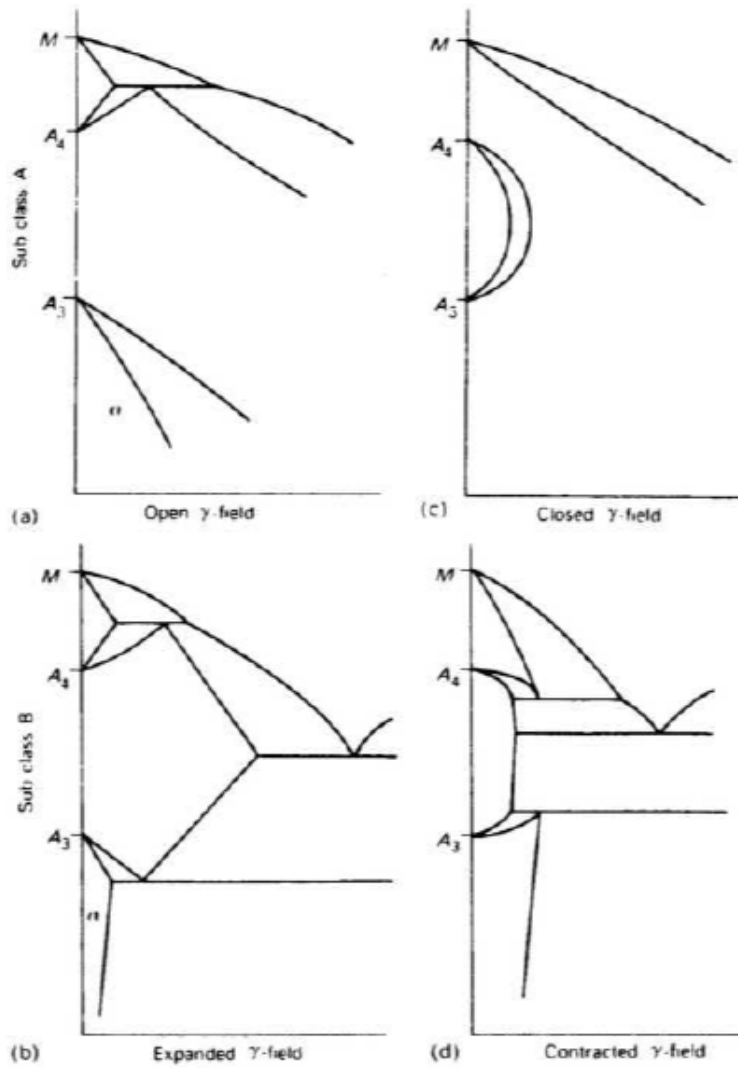
23

Figure 1.8: Classification of iron alloy phase diagrams : (a) open γ-field;
(b) expanded γ-field; (c) closed γ-field; (d) contracted γ-field. (Bhadeshia
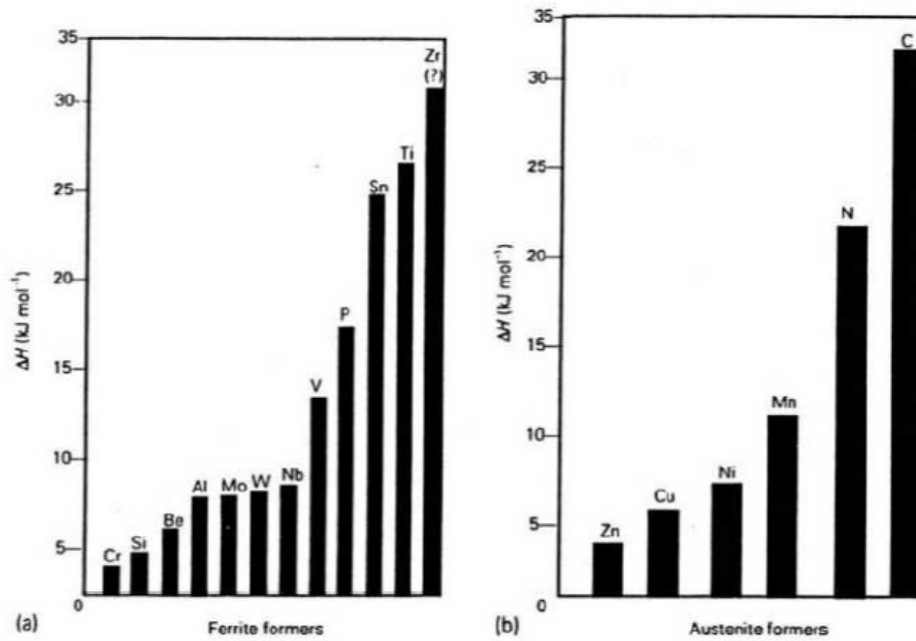and Honeycombe, 2006).

24

Figure 1.9: Relative strength of alloying elements as: (a) ferrite formers; (b) austenite formers (Bhadeshia and Honeycombe, 2006).

not continuously connected. Tantalum, niobium and zirconium fall within this class. From a thermodynamic point of view, open or expand austenite phase field means that the solute lowers the free energy of austenite. On the other hand, a closed or contracted γ-field imply alloying element stabilizes the formation energy of ferrite. The relative strength of alloying elements are shown in Fig 1.9.

The commonly researched Fe-Mn-Al-C light-weight steels contains 20 to

30 mass% manganese, 5 to 15 mass% aluminum and 1 to 3 mass% carbon. With these contents, the steel has austenite as the main phase. According to experimental work done by Ishida et al. (1990), when κ-carbide coexists with austenite, the minimum carbon content to form κ-carbide is higher than in the $\kappa + \alpha$ phase field. Because carbon solubility in austenite is larger than ferrite, sufficient carbon is available to form κ-carbide.

The experimental construction of a quaternary phase diagram is possible but it needs a lot of time, so alternative way have been developed. The CALPHAD (Computer coupling of phase diagrams and thermochemistry) assessment method requires thermodynamic databases and it is difficult for most of compounds to measure appropriate data. Therefore, a method to calculate basic thermodynamic data is needed and first-principles estimation is one solution.

When aluminum is used as alloying element, it my form various compounds, including, $FeAl_3$, Fe_3Al, Fe_3AlC, and Fe_2MnAlC. Thermodynamic data for these compounds are important to calculate a phase diagram, and there are reported values obtained using several method. Table 1.3 shows the calculation results and both first-principles calculation methods are for $0\,K$. The FLAPW calculation by Ohtani et al. (2004) has remarkable difference with other method. This results was explained by Connetable and Maugis (2008) to be a consequences poor convergence. To avoid that, they used very large

26

Compounds	CALPHAD assessment	FLAPW*	Pseudo Potential*
L1$_2$ Fe$_3$Al	-17.5[a], -19.3[b]	-8.8[c]	-19.3[d], -21.4[e]
E2$_1$ Fe$_3$AlC	-18.2[a], -16.0[b]	-27.9[c]	-18.4[e]
E2$_1$ Mn$_3$AlC	-27.3[a]	-	-

Table 1.2: Calculated results of formation enthalpy of L1$_2$ Fe$_3$Al, E2$_1$ Fe$_3$AlC and Mn$_3$AlC (in kJ/atom − mol).

The reference states are bcc Fe, fcc Al, cbcc Mn and graphite C.

[a] Chin et al. (2010)

[b] Connetable et al. (2008)

[c] Ohtani et al. (2004)

[d] Lechermann et al. (2005)

[e] Connetable and Maugis (2008)

* These are first-principles calculations but have different schemes for the atomic potentials. A detailed account will be given in chapter 2.5.

convergence parameters. Anyhow, these results are only for Fe-Al-C, and Mn-Al-C ternary systems. In the work of Chin et al. (2010), the results for Fe-Al-C and Mn-Al-C ternary systems was reproduced for Fe-Mn-Al-C quaternary system, and phase stability of κ-carbide, $(Fe,Mn)_3AlC$, in this quaternary system without the formation energy of Fe_2MnAlC and Mn_2FeAlC.

In first-principles calculations, formation energy calculations for adding, subtracting or replacing an atom is easier than other methods. However, first-principles calculations are for $0\,K$ making of hard to reproduce phase stability for realistic temperature ranges. Theoretically, the formation energy from first-principles calculation is accurate for $0\,K$ and vacuum environment. To extend the results, vibrational, electronic, and magnetic enthalpy and entropy increase should be considered. There have been numerous attempts to do this (Koermann et al., 2010; Liu, 2009; Ghosh et al., 2002; Kaufman et al., 2001; Turchi et al., 2005; Burton et al., 2001; Zhong et al., 2004; Turchi et al., 2007; Wang et al., 2004).

There are two additive properties which are lattice thermal vibrations and thermal electronic contributions. Thermal vibration is usually analyzed by the lattice dynamics or phonon approach, and the thermal electronic property can be neglected in some cases but if the density of states at the Fermi level is high, then thermal electronic contribution should be considered. In

28

Alloy (at.%)	Phase	Chemical composition (at.%)			
		Fe	Mn	Al	C
Fe-26Mn-13Al-8C	γ	54.3	26.1	12.7	6.9
	κ	40.4	28.1	15.9	15.6
Fe-26Mn-15Al-8C	γ	54.0	25.1	14.4	6.5
	κ	42.1	26.5	17.1	14.3
Fe-25Mn-17Al-8C	γ	52.3	25.1	16.5	6.1
	κ	42.3	25.9	18.7	13.1

Table 1.3: Chemical compositions evaluated by EPMA for γ and κ phases (Kimura et al., 2004).

addition, contributions from electron spin polarization should be included for magnetic materials. The mixing of different atoms needs to be taken into account in the total entropy.

κ-carbide forms by spinodal decomposition (Han and Choo, 1989; Sato et al., 1990; Choo et al., 1997; Chen et al., 2010a,b; Chang et al., 2010) and, in the work done by (Kimura et al., 2004), their Electron Probe Micro-Analyzer (EPMA) results show that κ-carbide has much more carbon than austenite has (Table 1.3). Suppose that Fe, Mn, Al atoms are at the same position in the both of austenite and κ-carbide, then, the only difference between austenite and κ is the existence and position of carbon. Also, man-

ganese and aluminum are substitutional solutes they diffuse more slowly than interstitial atoms like carbon so they will not move. Therefore, the results in table 1.3 could mean that only the carbon position and kinetics decide how κ-carbide forms. To confirm this theory, in this paper, the formation energy calculation for three different kinds of carbon octahedral interstice position was performed. Detailed information about the type of octahedral is in section 1.2.2. With this result, the Helmholtz free energy as a function of temperature was calculated by using Monte-Carlo simulations.

1.4   Previous Work

In section 1.3, there was an issue about the convergence of calculation results (Ohtani et al., 2004; Connetable and Maugis, 2008). So, before performing calculation, convergence parameters were tested for better performance. As a result, in this work, the calculation parameter for convergence was used by following the published work done by Seo et al. (2009).

2   First-Principles Calculation

First-principles, or *ab initio* calculation means that the calculation starts
directly from the fundamental laws of physics and doesn't use any assump-
tion like empirical method and fitting parameter.

The first-principles calculation has become the center of interest in many
field. So, in these days, from the semiconductor science to metallurgy, the
first-principles calculation is widely used.

The accuracy of first-principles calculation is guaranteed by the physics
theory. Also, it can calculate from a monatomic system to few hundred
atoms system is easy so it makes possible to study various possibility that
experiment cannot do.

2.1   Density Functional Theory (DFT)

Density functional theory (DFT) is the main stream to solve the Schrödinger
equation in first-principles calculation. DFT became very popular in quan-
tum chemistry since 1990s, because of a useful balance between accuracy
and computational cost in the solid state physics. DFT make the scientist
can calculate much larger systems than traditional *ab initio* method. In
many electron system, Schrödinger equation is Eq. (2.2) where, $e^2 = \hbar = m_e = 1$, the H is the hamiltonian of the system, Ψ is the wave function

and $\mathbf{r}_i$ denotes the position vector of electron.

$$H\Psi(\mathbf{r}_1, \mathbf{r}_2, \ldots, \mathbf{r}_n) = E\Psi(\mathbf{r}_1, \mathbf{r}_2, \ldots, \mathbf{r}_n) \qquad (2.1)$$

this can be written explicitly as

$$\{\sum_{i=1}^{n} -\tfrac{1}{2}\nabla_i^2 + \sum_{i=1}^{n} v_{ext}(\mathbf{r}_i) + \sum_{i<j}^{n} v_{ee}(\mathbf{r}_i, \mathbf{r}_j) + \sum_{i=1}^{n} v_{XC}(\mathbf{r}_i)\}\Psi(\mathbf{r}_1, \mathbf{r}_2, \ldots, \mathbf{r}_n)$$
$$= E\Psi(\mathbf{r}_1, \mathbf{r}_2, \ldots, \mathbf{r}_n)$$
$$(2.2)$$

The first term of left in the equation is kinetic energy of electrons, the second term v_{ext} is external potential by atom and the v_{ee} is electron-electron interaction, and the v_{XC} is exchange-correlation potential due to the Pauli's exclusion principle and correlation energy which is remaining unknown piece of energy. n is the number density of electron which is larger than Avogadro's number in solid. Solving the Schrödinger equation directly is hard because, it is too complicate to calculate, so, we need a suitable approximation which is called density functional theory.

2.2 The Variational Principle

The way to find ground state energy is provided by one simple principle called 'variational principle'. In the quantum mechanics, total energy of the system with hamiltonian $\hat{H}$, can be expressed by Eq. (2.3).

$$E = \min_{\phi} < \phi | \hat{H} | \phi > \tag{2.3}$$

Where, the ϕ is the wave function which satisfies,

$$\int_{-\infty}^{\infty} dx |\phi(x)|^2 = 1 \tag{2.4}$$

This equations mean that any normalized trial wave function can be used to find ground state energy of the system and only one wave function is satisfy the minimum energy (See section 2.3). Therefore, the total energy calculation result is always same or lager than true ground state energy, in the same meaning, the lower energy is the more accurate energy.

2.3 Hohenberg-Kohn Theorems

Hohenberg-Kohn theorems are result of the formulation of density functional theory as an exact theory of many-body systems. The first theorem shows that only from the ground state density, $n_0(\mathbf{r})$, all properties of of the system can be determined. This theorems complete the loop between external potential $V_{ext}(\mathbf{r})$, wave function of all state $\Psi_i(\{\mathbf{r}\})$ and ground state wave function $\Psi_0(\{\mathbf{r}\})$. Fig. 2.1 shows schematic description of Hohenberg-Kohn theorem (Hohenberg and Kohn, 1964).
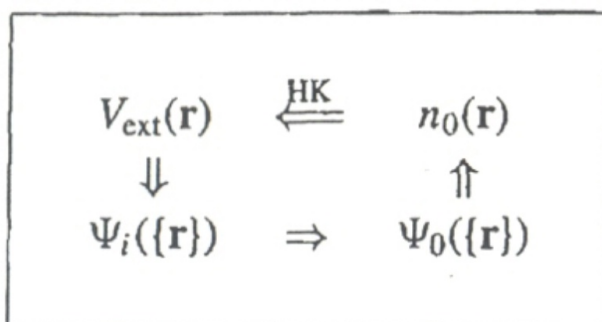
Figure 2.1: Schematic representation of Hohenberg-Kohn theorem. The smaller arrows denote the usual solution of the Schrödinger equation where the potential $V_{ext}(\mathbf{r})$ determines all states of the system $\Psi_i(\{\mathbf{r}\})$, including the ground state $\Psi_0(\{\mathbf{r}\})$ and ground state density $n_0(\mathbf{r})$. The long arrow labeled "HK" denotes the Hohenberg-Kohn theorem, which completes the circle (Martin, 2004).

2.4 The Kohn-Sham Equation

The Kohn-Sham equation is widely used for most "first-principles" or "*ab initio*" calculation tools for atoms, molecules, and condensed matter.

Unlikely to Hohenberg-Kohn theorems, the Kohn-Sham equation is the approach to make problem simple by a mathematical assumptions. The result in shown in Eq. (2.5).

$$\{-\frac{1}{2}\nabla^2 + v_s(\mathbf{r})\}\psi_i(\mathbf{r}) = \epsilon_i\psi_i(\mathbf{r}) \tag{2.5}$$

where,

$$v_s(\mathbf{r}) = v_{ext}(\mathbf{r}) + \int d^3r \frac{n(\mathbf{r})}{|\mathbf{r} - \mathbf{r}'|} + v_{XC}[n](\mathbf{r}) \qquad (2.6)$$

and the density of electron,

$$n(\mathbf{r}) = \sum_{i=1}^{n} |\psi_i(\mathbf{r})|^2 \qquad (2.7)$$

where the ψ_i is the one-particle wave function. Now, the many-body Schrödinger equation becomes non-interacting single electron equation.

In the published work by Kohn and Sham in 1965 (Kohn and Sham, 1965), their *ansatz* assumes that the ground state density of many-body interacting system is equal to that of some single particles non-interacting system. The specific result is shown in Eq. (2.2) to Eq. (2.6). Fig. 2.2 shows the schematic diagram of Kohn-Sham equation.

While the Kohn-Sham equation change the problem from interacting system to non-interacting system, the difficulty of many-body problem is concentrated to deal with the exchange-correlation functional in Eq. (2.6).

2.4.1 Local Density Approximation (LDA)

Local density approximation (LDA), or more generally local spin density approximation, is the widely used method to calculate exchange-correlation energy in the Kohn-Sham equation. In the LDA, the exchange-correlation
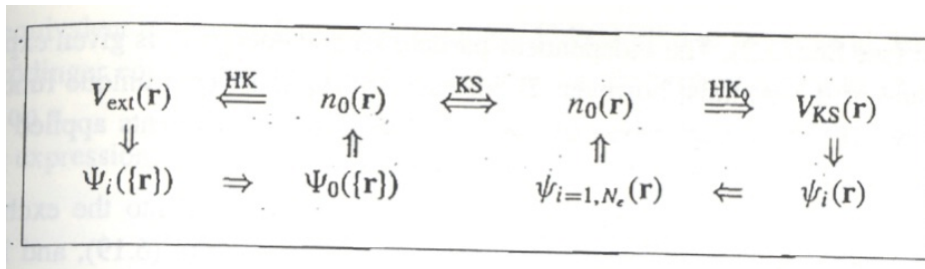
$$V_{ext}(\mathbf{r}) \quad \overset{HK}{\Longleftarrow} \quad n_0(\mathbf{r}) \quad \overset{KS}{\Longleftrightarrow} \quad n_0(\mathbf{r}) \quad \overset{HK_0}{\Longrightarrow} \quad V_{KS}(\mathbf{r})$$
$$\Downarrow \qquad\qquad \Uparrow \qquad\qquad \Uparrow \qquad\qquad \Downarrow$$
$$\Psi_i(\{\mathbf{r}\}) \quad \Rightarrow \quad \Psi_0(\{\mathbf{r}\}) \qquad \psi_{i=1,N_e}(\mathbf{r}) \quad \Leftarrow \quad \psi_i(\mathbf{r})$$

Figure 2.2: Schematic representation of Kohn-Sham *ansatz*. (Compare to Fig. 2.1.) The notation HK_0 denotes the Hohenberg-Kohn theorem applied to the non-interacting problem. The arrow labeled KS provides the connection in both directions between the many-body and independent particle systems, so that the arrows connect any point to any other point. Therefore, in principle, solution of the independent particle Kohn-Sham problem determines all properties of the full many-body system (Martin, 2004).

energy is an integral over all space with exchange-correlation energy density at each point assumed to be the same as in a homogeneous gas with that density.

2.4.2 Generalized Gradient Approximation (GGA)

In the LDA method, exchange-correlation potential was assumes to be the equal as in a homogeneous gas with that density. In the generalized gradient approximation, the functional of the gradient of density $|\nabla n|$ is used. So GGA can be dealing with inhomogeneous system. Indeed, It is easy to composite to program. By GGA, exchange-correlation functional can be

expressed by Eq. 2.8.

$$
\begin{aligned}
E_{XC}^{GGA}[n^\uparrow, n^\downarrow] &= \int \mathrm{d}^3 r \, n(\mathbf{r}) \epsilon_{XC}(n^\uparrow, n^\downarrow, |\nabla n^\uparrow|, |\nabla n^\downarrow|, \dots) \\
&\equiv \int \mathrm{d}^3 r \, n(\mathbf{r}) \epsilon_X^{hom}(n) F_{XC}(n^\uparrow, n^\downarrow, |\nabla n^\uparrow|, |\nabla n^\downarrow|, \dots)
\end{aligned}
\tag{2.8}
$$

where, $n^\uparrow$ and $n^\downarrow$ is the density of each spin, ϵ_{XC} is exchange-correlation energy, F_{XC} is dimensionless and ϵ_X^{hom} is the exchange energy of the unpolarized gas.

2.5 All Electron Full Potential Linearized Augmented Plane Wave Method (FLAPW)

There are many methods in the world to solve the Kohn-Sham equation and they are distinguished by how they deal with each term in the left of Eq. 2.2. The categorized DFT implementations are shown in Fig. 2.3.

In this research, self-consistent all-electron full potential linearized augmented plane wave method (FLAPW) and GGA was used. The FLAPW, in the condensed matter, divide the unit cell by three different type; muffin-tin sphere, interstitial regions between the spheres and vacuum. Muffin-tin (MT) spheres are located in nuclei of each atoms. Fig. 2.4 shows the schematic geometry in FLAPW calculation, where R_{MT} denotes the radius
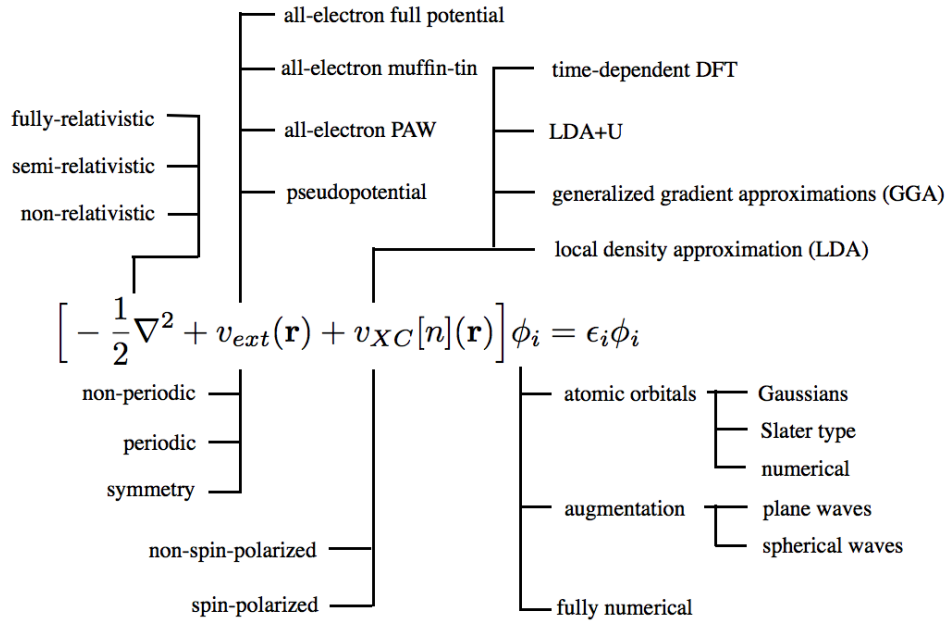
37

all-electron full potential

all-electron muffin-tin

all-electron PAW

pseudopotential

time-dependent DFT

LDA+U

generalized gradient approximations (GGA)

local density approximation (LDA)

fully-relativistic

semi-relativistic

non-relativistic

$$\left[-\frac{1}{2}\nabla^2 + v_{ext}(\mathbf{r}) + v_{XC}[n](\mathbf{r}) \right]\phi_i = \epsilon_i\phi_i$$

non-periodic

periodic

symmetry

non-spin-polarized

spin-polarized

atomic orbitals — Gaussians

Slater type

numerical

augmentation — plane waves

spherical waves

fully numerical

Figure 2.3: Categorized DFT implementations (Blugel, 2010).

of muffin-tin sphere.

The FLAPW method use full potential, not approximate the shape of charge density and potential so, to calculate ground state energy, trial wave function in the variational principle (section 2.2) will be complicated. However, the psuedopotential method approximate the atomic potential. As a result, trial function is also simple.

Plane wave functions and its sum are naturally orthonormal to each other,
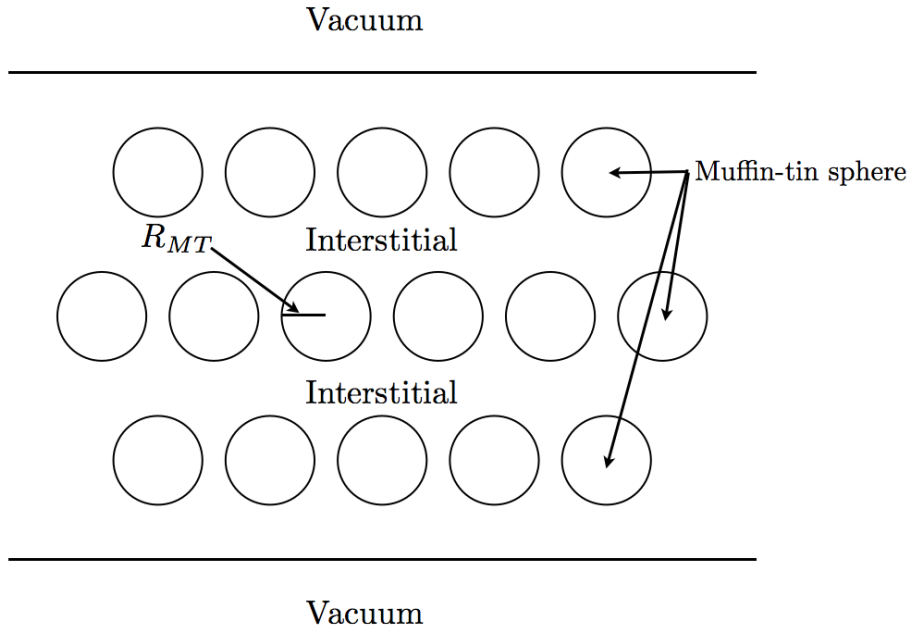
Figure 2.4: Geometry of FLAPW, where R_{MT} denotes the radius of muffin-tin sphere.

so FLAPW uses plane wave function as a basis set of one-particle wave function in the Kohn-Sham equation (Eq. (2.5)). Therefore, FLAPW one-particle wave function in the geometry are

$$\psi_i(\mathbf{r}, \mathbf{k}) = \sum_j c_{ij} \phi(\mathbf{r}, \mathbf{K}_j); \quad \mathbf{K}_j = \mathbf{k} + \mathbf{G}_j \qquad (2.9)$$

where, $\mathbf{k}_{||}$ is an arbitrary vector of the Brillouin zone (BZ) and $\mathbf{G}_j$ is a three-dimensional (3D) reciprocal lattice vector. Then, the basis functions in each partition in FLAPW geometry are:

$$\phi(\mathbf{r}, \mathbf{K}_j)$$
$$= \begin{cases} \Omega^{1/2} e^{i\mathbf{K_j}\cdot\mathbf{r}} & \text{interstitial} \\ \sum_{lm}^{\alpha}[A_{lm}^{\alpha}(\mathbf{K}_j)u_l(E_l^{\alpha}, r_{\alpha}) + B_{lm}^{\alpha}(\mathbf{K}_j)\dot{u}_l(E_l^{\alpha}, r_{\alpha})]Y_{lm}(\hat{r}_{\alpha}) & \text{sphere} \\ \sum_q[A_q(\mathbf{K}_j)u_{kq}(E_{\nu}, z) + B_q(\mathbf{K}_j)\dot{u}_{kq}(E_{\nu}, z)]e^{i(\mathbf{k}+\mathbf{K}_q)\cdot\mathbf{r}} & \text{vacuum} \end{cases}$$
$$(2.10)$$

where, u_l is the solution of the radial Schrödinger equation solved at a fixed energy parameter E_l and their derivatives $\dot{u}_l$. The Y_{lm} are spherical harmonics at quantum number l and m, and the coefficients A_{lm} and B_{lm} are determined by the requirement that the plane waves be continuous in value, as be their radial derivative, at the atomic spheres.

2.6   Computational Method

The Kohn-Sham equation (Kohn and Sham, 1965) was solved self-consistently by the all-electron total-energy full potential linearized augmented plane wave (FLAPW) method (Weinert et al., 1982; Wimmer et al., 1981) implemented in the QMD-FLAPW package within the generalized gradient approximation (Perdew et al., 1996) to density functional theory (Hohen-

40

berg and Kohn, 1964). The integration over the three dimensional Brillouin zone (3D-BZ) was performed by the improved tetrahedron method (Lee et al., 2002) over $21 \times 21 \times 21$ for κ-carbide and another carbon octahedral position, diamond carbon, FCC Al, FCC manganese, and BCC Fe Monkhorst-Pack mesh (Monkhorst and Pack, 1976) in the 3D-BZ. The linearized augmented plane wave (LAPW) basis set was expanded by using a plane wave cutoff $K_{\max}$, which was $7.7 \times 2\pi/a$ where a is the lattice constant for the corresponding system. Lattice harmonics with $l \leq 10$ were employed to expand the charge density, potential and wave functions inside each muffin-tin sphere, with the radii of 2.0 a.u. for Fe, Al, and Mn and 1.3 a.u. for C atom. The star-function cutoff, $G_{\max}$, was set by $3 \times K_{\max} = 23.1 \times 2\pi/a$. $G_{\max}$ was employed for depicting the charge density and potential in the interstitial region. In this research, all calculation parameters are based on work done by Seo et al. (2009). The core electrons were treated fully relativistically while valence states were treated scalar relativistically without spin-orbit coupling. Self-consistency was assumed when the difference between input and output charge (spin) density was less than 1.0×10^{-5} electrons/a.u.[3] The equilibrium volume and bulk modulus are obtained by fitting to the Murnaghan equation of state (Murnaghan, 1937).

All of calculated materials is optimized with respect to its lattice parame-

ter.

Calculated total energy of the system is the internal energy U at zero Kelvin and zero pressure. The formation enthalpy ΔH at zero Kelvin and zero pressure is the calculated internal energy ΔU as and product of volume V and external pressure P vanish at zero pressure. The formation enthalpy of a ternary quaternary compound $W_k X_l Y_m Z_n$, $\Delta H_f(W_k X_l Y_m Z_n)$ is

$$\Delta H_f(W_k X_l Y_m Z_n) = \frac{\{U(W_k X_l Y_m Z_n) - kU(W) - lU(X) - mU(Y) - nU(Z)\}}{k + l + m + n}$$

(2.11)

where W, X, Y, and Z are elements and k, l, m, and n are the number of W, X, Y, and Z atoms, respectively.

3 Monte-Carlo Simulation

Monte-Carlo simulation is the way that uses random sampling of the system to compute their result. Monte-Carlo is used for unfeasible or impossible to calculate an exact result because it is suitable for computation with its reliance on repeated computation of random numbers. Also, Monte-Carlo simulation is suitable for studying large number of coupled system, such as fluid, disordered materials and strongly coupled solid.

Wang-Landau method (Wang and Landau, 2001b), which is one of the Monte-Carlo method for statistical physics, was chosen for calculation scheme because it is naturally imply the temperature dependence of system. In this research, first-principles calculation result, at zero Kelvin and zero pressure, is reassessed to finite temperature by Wang-Landau method.

3.1 Partition Function

The partition function is the important quantity that include the information of equilibrium statistical mechanics. From the partition function, it is possible to derive essential information to figure out the properties of the system such as free energy, internal energy and entropy. The general form

for partition function for classical system Z is

$$Z = \sum_{\text{all states}} e^{-\mathcal{H}/k_\text{B}T} \qquad (3.1)$$

where $\mathcal{H}$ is the Hamiltonian of the system, T is temperature, and k_B is the Boltzmann constant. In general, partition function cannot be computed exactly because it is too big to calculate by computer. For example, for 10000 interacting atoms with two possible states per atom, the partition function of given system would contain 2^{10000} terms. The probability of any possible state of system is also acquired from the partition function. The probability that state is in particular state μ is given by

$$P_\mu = e^{-\mathcal{H}(\mu)/k_\text{B}T}/Z \qquad (3.2)$$

where, $\mathcal{H}(\mu)$ is the Hamiltonian when the system is in the μth state.

3.2 Free Energy, Internal Energy, Specific heat and Entropy

Partition function is directly connected with thermodynamic quantities, such as, Free energy, Internal energy and Entropy. The Helmholtz free energy of the system can be determined by partition function from,

$$F = -k_\text{B}T \ln Z \qquad (3.3)$$

44

then, other thermodynamic properties can be calculated by differentiation of Eq. 3.3. The internal energy U of the system can be obtained from the free energy via

$$U = -T^2 \frac{\partial}{\partial T}\left(\frac{F}{T}\right)$$ (3.4)

or, from the partition function,

$$U = \frac{\sum_\mu E_\mu e^{-\mathcal{H}/k_\mathrm{B}T}}{Z} = \langle E \rangle_T$$ (3.5)

The specific heat can be estimated from the fluctuations in the internal energy (Wang and Landau, 2001a)

$$C(T) = \frac{\langle E^2 \rangle_T - \langle E \rangle_T^2}{k_\mathrm{B}T^2}$$ (3.6)

Also, the entropy S of the system is given by

$$S = k_\mathrm{B} \ln P$$ (3.7)

where P is the probability of the occurrence of a state. Then, the entropy can be determined from the free energy from

$$S = -\left(\frac{\partial F}{\partial T}\right)_{V,N}$$ (3.8)

where V is the volume of the system and N is the composition.

3.3   Metropolis method

The Metropolis Monte-Carlo algorithm (Metropolis et al., 1953) was initiated from Boltzmann's insight that in the finite temperature, molecules are distributed between high energy or unfavorable states and low energy or favorable states.

In the Metropolis method,

In the Metropolis method, it has one reference state (A) and make one "reference candidate" state (B) randomly. Then it compares the energy of the each state and it changes reference state by following rule.

1. if $E_A \geq E_B$ then B become reference state.

2. if $E_A \leq E_B$ then, generate random number P in range $0 \leq P \leq 1$. Then, compare P with $\exp(-\Delta E/k_B T)$, if $P \leq \exp(-\Delta E/k_B T)$, B is the reference state, if it's not, A is the reference state.

where E_A and E_B are energies of the states A and B, and $\Delta E = E_B - E_A$. Therefore, the system can be unfavorable state or high energy state. After enough number of iteration, the reference state would become arithmetic averages over the entire sample of states.

3.4 Wang-Landau method

The Wang-Landau method is the extension of the Metropolis method to develop for calculate the density of states of a computer simulated system, such as Ising model of spin glasses, or model atoms in a molecular force field (Wang and Landau, 2001a,b; Landau et al., 2004). The possibility that decide what states the molecules belong to is given by energy difference and the density of states.

The difference between Metropolis and Wang-Landau methods is how they change the reference state.

In the method, firstly, the minimum and maximum possible states are calculated and divided by given number to make a histogram. A visits histogram $H(E)$ is initially 0 for all states. In the Wang-Landau method, it uses density of the states $g(E)$ so, changing state is accepted when,

$$P < \min \left\{ 1, \frac{g(E_A)}{g(E_B)} \right\} \tag{3.9}$$

where, the generated random number P is on $[0, 1)$. Density of the states $g(E)$ is all 1 at the first time. Also, Wang-Landau method use update factor f which is initially e and reduced to square root of itself after end of the iteration.

Also, every "reference candidate" state are recorded in visits histogram

$H(E)$, for instance, in the method, it already divided energy range. If the generated state B is in some n-th energy range ΔE_n, then histogram at ΔE_n will increase by 1. Similarly, At the first time, the density of states $g(E)$ is unknown so all density of states are set to 1. Typically, density of states is very large for some states therefore log space. $g(E)$ is also increased by update factor f. In the Wang-Landau method, every iteration ends when $H(E)$ is "flat" and whole calculation finish after $f < 10^{-8}$. From the calculated $g(E)$, the partition function Z can be earned by

$$Z = \sum_{E_i} P(E_i) \tag{3.10}$$

where,

$$\ln P(E_i) = \ln g(E_i) - E_i/k_{\mathrm{B}}T \tag{3.11}$$

In this research, both methods were mixed because there is no specific criterion of end of simulation in Metropolis method and no temperature dependence in Wang-Landau method when it compare the states. Therefore, the method in this research used temperature dependence of the state from Metropolis method and simulation terminate criterion from Wang-Landau method.

Monte-Carlo simulation was deal with $10 \times 10 \times 10$ unit cells as shown in

Fig 4.21. Each cells can change the state such as non-magnetic or spin polarized Fe_2MnAlC octa-1 to octa-3. Simulation followed procedure in below.

1. Set the temperature T and set visits histogram $H(E)$ as 0, density of the states $g(E)$ as 1 for all energies and set update factor $f = e$.

2. Give the random states for each cells and call it reference state A and its energy is denoted by E_A.

3. Make random "candidate" state and call it B and its energy is denoted by E_B.

4. if $E_A \leq E_B$ then, generate random number P in range $0 \leq P \leq 1$. Then, compare P with $\exp(-\Delta E/k_BT)$, if $P \leq \exp(-\Delta E/k_BT)$, B is the reference state, if it's not, A is the reference state.

5. Increase $H(E_B)$ by 1 and $g(E_B)$ by f.

6. If $H(E)$ is "flat", set $H(E)$ to 0 for all energies and set f as $\sqrt{f}$.

7. Go back to procedure 3, while f becomes smaller than 10^{-8}.

To program this algorithm, C++ was used as a programing language.

4 Results and Discussions

Importance of κ-carbide in light-weight steel is reviewed in chapter 1. Especially, effect of κ-carbide on mechanical properties of steels can be changed with size and position of κ-carbide, or whether it forms lamellar structure with other phases or not. There is remarkable results by Frommeyer and Brüx (2006). In their research, the specific energy absorption is as high as that of TWIP steels. This reflects that it is possible to reduce more density with good mechanical properties. For the TWIP and TRIP steels case, lowering density is limited because amount of aluminum affect to stacking fault energy so it could be lost its characteristic (Tian et al., 2008). Therefore, figuring out exact phase diagram of κ-carbide can improve the research about light-weight steel. In this research, first-principles calculation was performed with various κ-carbide such as Fe_3AlC, Fe_2MnAlC, $FeMn_2AlC$, and with this result, Monte-Carlo simulation in the finite temperature was also studied.

4.1 Lattice Parameter Optimization

κ-carbide has a anti-perovskite structure which shown in figure 1.2. Starting from the lattice constants in published work of Palatnik et al. (1964), the unit cell volume was extended and compressed to find equilibrium lat-

tice parameter with minimum energy. The minimum energy and equilibrium lattice parameter was fitted to the Murnaghan equation of state (Murnaghan, 1937). In this research, all possible carbon octahedral position in Fe_2MnAlC was calculated. After here, octa-1 denotes normal anti-perovskite (Fig 1.3 (a)), octa-2 denotes Fig 1.3 (b) and octa-3 denotes Fig 1.3 (c).

All of κ-carbides are calculated in spin-polarized condition because non-magnetic κ-carbide had higher energy than spin-polarized phase.

Table 4.1 shows the equilibrium lattice parameter of κ-carbide in this research and another literature. For Fe_3AlC, calculated lattice constant is 0.6% smaller than the experimental result. this is and excellent agreement with given data. Also, Fe_2MnAlC is well agreed with 0.2% larger than experimental data. In the experiment, amount of manganese is not as much as single Fe_2MnAlC, so two κ-carbides, Fe_3AlC and Fe_2MnAlC would be mixed. This could explain that why experiment measures smaller value. Because the experimental way to measure the lattice parameter such as transmission electron microscope (TEM) or X-ray diffraction is actually measure the distance between face to face which is the average of the lattice parameters. When the carbon octahedral position was changed to another octahedral position, table 4.1 shows lattice expansion for octa-2 and octa-3. The lattice constant of Fe_2MnAlC (octa-2) was increased by 1.7% with

51

	Calculated		Literature	
			Calculation	Experiment
	$a/\text{Å}$	$V/\text{Å}^3$	a / Å	
Fe$_3$AlC	3.759	53.1	3.677[a], 3.75[b]	3.781[c], 3.78[d]
Fe$_2$MnAlC (octa-1)	3.788	54.4	-	3.78[e] , 3.77∼3.79[f]
Fe$_2$MnAlC (octa-2)	3.854	57.2	-	-
Fe$_2$MnAlC (octa-3)	3.858	57.4	-	-
Mn$_3$AlC	3.815	55.5	-	-

Table 4.1: The calculated lattice parameter and volume of the unit cell of κ-carbide with various compositon.

octa-1 denotes normal anti-perovskite (Fig 1.3 (a)), octa-2 denotes

Fig 1.3 (b) and octa-3 denotes Fig 1.3 (c)

[a] Ohtani et al. (2004)

[b] Connetable and Maugis (2008)

[c] Palatnik et al. (1964)

[d] Palm and Inden (1995)

[e] Choo and Han (1985)

[f] Kimura et al. (2002)

	H / kJ atom-mol^{-1}
BCC Fe	-3.3411185×10^6
Graphite C	-1.0001125×10^5
FCC Al	-6.3740864×10^5
CBCC Mn	-3.0414821×10^6

Table 4.2: The calculated enthalpies of each atom as a reference in its pure crystal.

respect to octa-1 and octa-3 is 1.8% larger than octa-1. Also, increase of number manganese atom in the unit cell made the lattice expand.

4.2   Formation Enthalpy

The formation enthalpy at zero Kelvin and zero pressure (ΔH) of Fe$_{3-x}$Mn$_x$AlC system, where x is the number of manganese atom in the κ-carbide, was calculated using first-principles to figure out thermodynamic properties when number of Mn was changed. Each Fe$_{3-x}$Mn$_x$AlC system was optimised with respect to lattice constant by using first-principles calculation as shown in Table 4.1. To calculate formation enthalpy, enthalpy of reference state of each atom is needed. In this research, body centered cubic (BCC) iron, face centered cubic (FCC) aluminium, complex body centered cubic (CBCC) manganese, and graphite carbon were calculated as refer-

ence states. All reference states were optimised with respect to lattice constant using first-principles calculation. In the first-principles calculation, van der Waals interaction is not reliably calculated. Instead, diamond carbon was calculated. The enthalpy of graphite was calculated by subtract the graphite-diamond enthalpy difference $1.895\,\text{kJ/atom-mol}$ (Franke and Neuschutz, 2002; Barin, 2004). Also, The cbcc Mn or α-Mn has non-colinear magnetism which is hard to converge so, fcc Mn was calculated then, the energy difference between cbcc or α-Mn and fcc or γ-Mn $6.8\,\text{kJ/atom-mole}$ was subtracted to their value (Hobbs and Hafner, 2001). Table 4.2 shows the calculated enthalpies of the pure state of each atom.

The formation enthalpies of $Fe_{3-x}Mn_xAlC$ which were calculated by following Eq. 2.11 were shown in Table 4.3. All the calculated formation enthalpy were negative, except the Fe_2MnAlC (octa-2) and Fe_2MnAlC (octa-3). Most stable state of the κ-carbide is Fe_2MnAlC (octa-1) with the formation enthalpy of $-24.8\,\text{kJ atom-mol}^{-1}$, which is $6.6\,\text{kJ atom-mol}^{-1}$ lower than Fe_3AlC and $4.8\,\text{kJ atom-mol}^{-1}$ less than Mn_3AlC. This results reflects that the stability of κ-carbide in the Fe-Mn-Al-C quaternary system.

Calculated formation enthalpy in this research has higher value than another first-principles calculation. The result of Ohtani et al. (2004) is much lower than the other values. This was explained by its poor convergency. To avoiding this convergency problem caused by calculation parameters, the

	ΔH / kJ atom-mol^{-1}		
	Calculated	CALPHAD method	first-principles calculations
Fe$_3$AlC	-16.7	-18.2^{a}, -16.0^{b}	-27.9^{c} , -18.4^{d}
Fe$_2$MnAlC (octa-1)	-24.8	-	-
Fe$_2$MnAlC (octa-2)	7.74	-	-
Fe$_2$MnAlC (octa-3)	6.20	-	-
Mn$_3$AlC	-20.0	-27.3^{a}	-

Table 4.3: Calculated formation enthalpy ΔH of Fe$_{3-x}$Mn$_x$AlC

The reference states are bcc Fe, fcc Al, cbcc Mn and graphite C in this research.

[a] Ref. (Chin et al., 2010)

[b] Ref. (Connetable et al., 2008)

[c] Ref. (Ohtani et al., 2004)

[d] Ref. (Connetable and Maugis, 2008)

convergence test was investigated and published (Seo et al., 2009). All cal-
culation parameters in this research followed the result of that convergence
test.

	Total magnetization
	(T)
Fe$_3$AlC	0.675
Fe$_2$MnAlC (octa-1)	0.838
Fe$_2$MnAlC (octa-2)	1.28
Fe$_2$MnAlC (octa-3)	1.26
Mn$_3$AlC	0.822

Table 4.4: Calculated total magnetization in the unit of Tesla (T).

4.3   Magnetism

Magnetism in Fe-Mn-Al-C was researched to figure out the relationship between magnetism and stacking fault energy. There is published report by Tian et al. (2008). In their literature, they researched antiferromagnetic order on SFE in the austenitic Fe-Mn-Al-C alloys. Also, magnetic contribution on entropy is important when establish thermodynamic model for magnetic element such as iron or manganese. So, Ohtani et al. (2004) considered magnetic contribution when they calculate Gibbs free energy (Ohtani et al., 2004). In this section, the magnetism of each κ-carbide was studied such as magnetic moment of unit cell, total magnetization and magnetic moment of individual atom.

	Spin magnetic moment of the atom (μ_B)				
	Al	C	Fe(1)	Fe(2)	Mn
Fe_3AlC	-0.06	-0.07	1.11	-	-
Fe_2MnAlC (octa-1)	-0.07	-0.08	1.25	-	1.62
Fe_2MnAlC (octa-2)	-0.04	-0.01	1.46	-	3.23
Fe_2MnAlC (octa-3)	-0.04	-0.06	2.58	1.80	1.92
Mn_3AlC	-0.05	-0.08	-	-	1.29

Table 4.5: Calculated magnetic moment of the atom in the muffin-tin sphere.

Table 4.4 and table 4.5 shows the calculated total magnetic moment per unit cell, total magnetization and magnetic moment of each atoms. Magnetic moment per unit cell was increased when Mn atom substitute Fe atoms, but when all Fe atoms were substituted by manganese atoms, the magnetic moment decrease $0.016\,T$ than Fe_2MnAlC (octa-1). Carbon octahedral position in Fe_2MnAlC affects greatly on total magnetization. In the octa-2 and octa-3 structure, The Fe or Mn atoms without the nearest-neighbor bonding with the C atom have much increase magnetic moments of $1.33\,\mu_B$ and $1.61\,\mu_B$, for Fe and Mn atoms, respectively (See Fig 1.3). In the table 4.5, Mn atom in octa-2 have more than twice magnetic moment

with respect to Mn in Mn_3AlC and same result was shown on Fe atoms in octa-3 and Fe_3AlC.

4.4 Electronic structure

Fig 4.1 to Fig 4.10 shows the band structure of Fe_3AlC, Mn_3AlC, Fe_2AlC octa-1, Fe_2AlC octa-2 and Fe_2AlC octa-3, where, the E_f denotes the fermi energy which is the energy when all electrons occupies the band and density of the states at $0\,K$. The fermi enery is set to be zero. Fig 4.13 to 4.20 shows the density of the states (DOS) of each atom in κ-carbides.

In the band structure of Fe_3AlC (Fig 4.1 and Fig 4.2), there are flat d-bands on the fermi energy between Γ and X. The electron in these band is very sensitive to external stimulation. However, If all of Fe atoms are substituted by Mn atoms like Mn_3AlC (Fig 4.3 and Fig 4.4), The flat band moves above the fermi level and there in no more flat band on the fermi level. So, this explains why the formation energy of Mn_3AlC is lower than Fe_3AlC. This phenomena happens because Mn atom have one less electrons than Fe atom. Also in Mn_3AlC, it is possible to observe the distance between the bands become larger than those of Fe_3AlC. This can be explained by repulsion because of Mn atom. For the Fe atom, all electrons have pairs but Mn atom has odd number electron. Therefore, there is repulsion between bands due to spin and it makes wider band structure. For Fe_2MnAlC (octa-1) case (Fig 4.5 and Fig 4.6), one substitution of Mn atom only affects spin-down band structure compared to Fe_3AlC. The substitution remove the flat band on the fermi level, and repulsion between band

59

is smaller than Mn_3AlC. With this result, Fe_2MnAlC (octa-1) is the most stable structure.

From the point of DOS, around the $-3.5\,eV$ in total DOS of Fe_3AlC, Mn_3AlC and Fe_2MnAlC (octa-1), there is strong hybridization (or peak) between p-Al, p-C and d-Fe or d-Mn orbitals (Fig 4.11, Fig 4.13, Fig 4.15, Fig 4.17 and Fig 4.19). This hybridization can be explained by the position of the iron and manganese atoms, i.e. in the directions of the p-C and p-Al orbitals. When carbon octahedral position changed, that strong hybridization is decreased because p-Al and p-C make hybridization instead of Fe or Mn, so peak near the $-3.5\,eV$ is vanished in Fig 4.12. Instead of that peak, DOS was increased in the range from $-3\,eV$ to $2\,eV$. In the energetic point of view, Fe_3AlC, Mn_3AlC and Fe_2MnAlC is preferred more than Fe_2MnAlC (octa-2) and Fe_2MnAlC (octa-3).
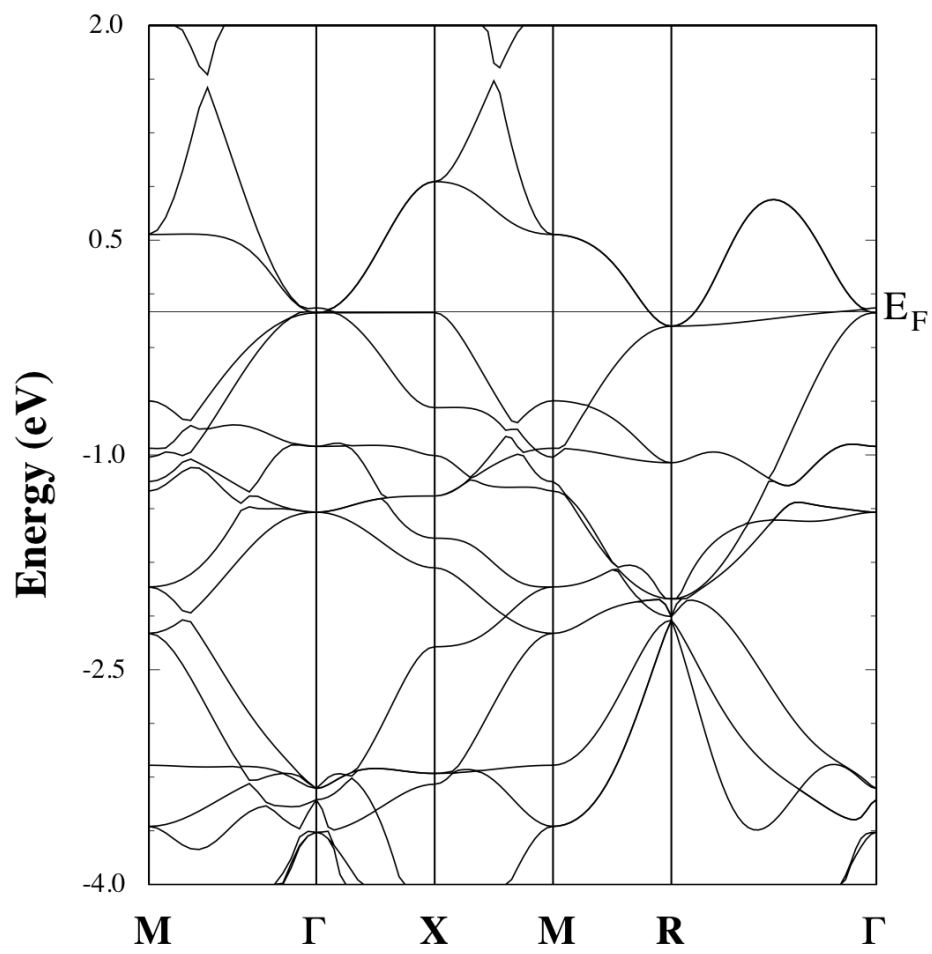
Figure 4.1: Band figure for spin-up of Fe$_3$AlC.
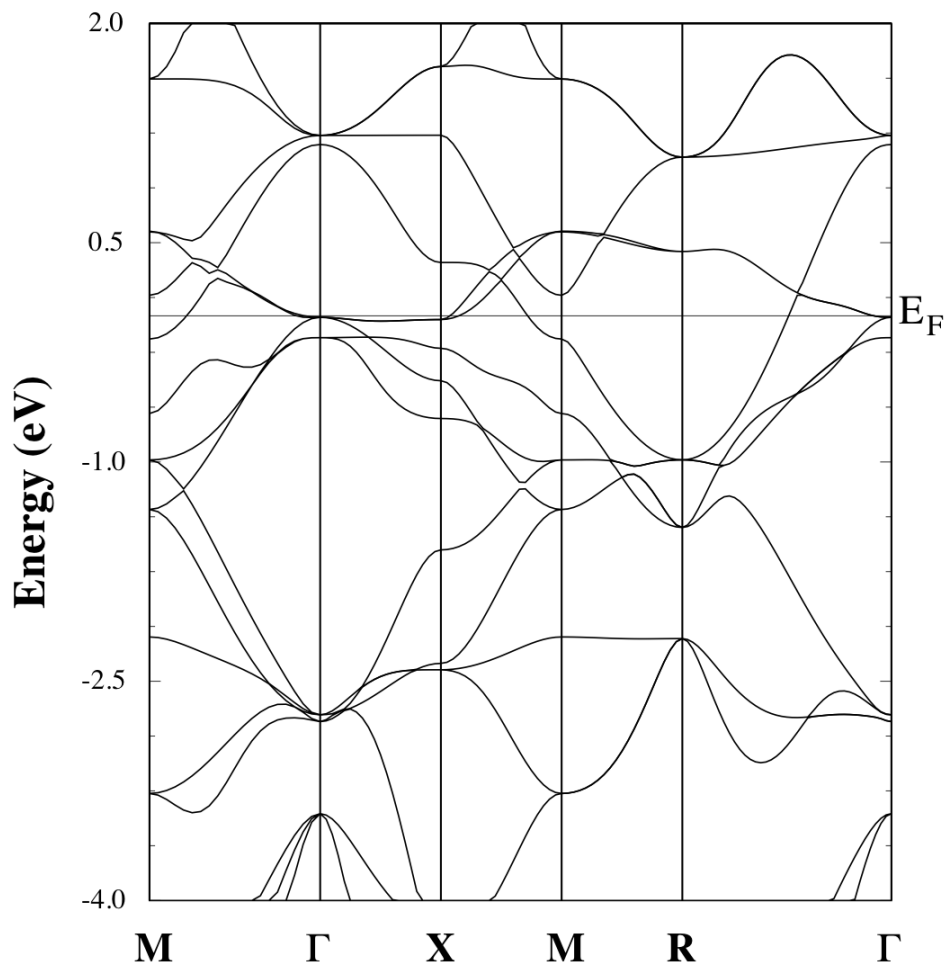
Figure 4.2: Band figure for spin-down of Fe$_3$AlC.
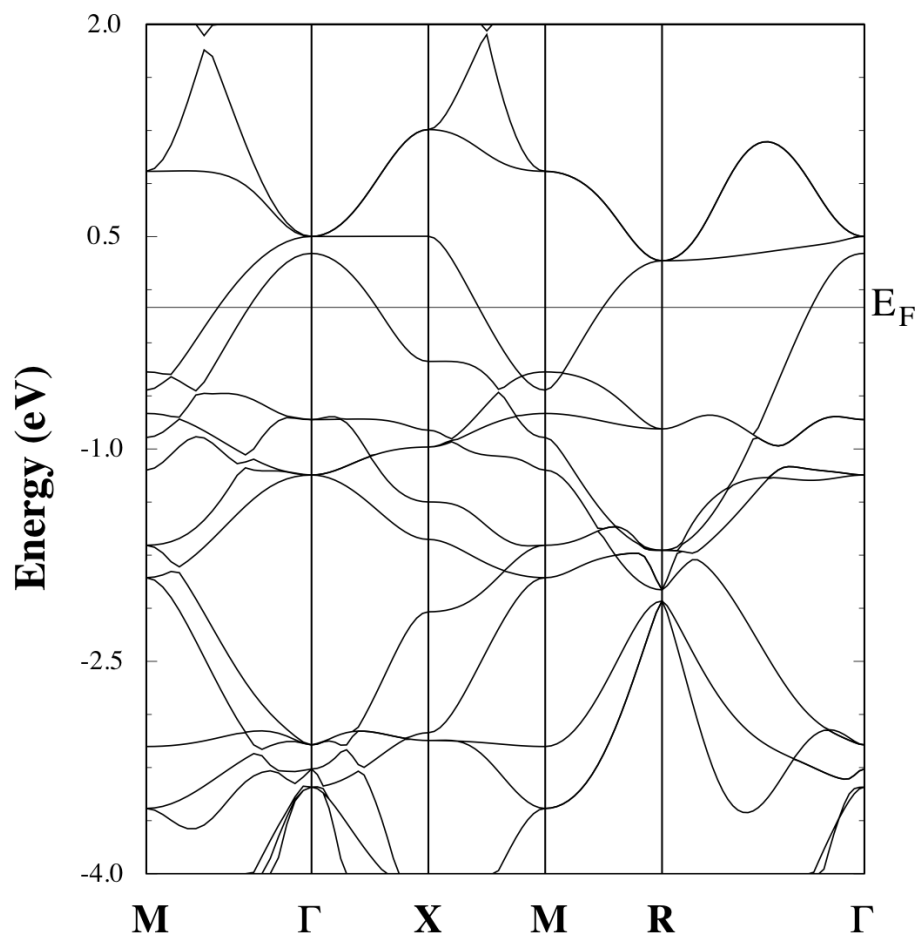
Figure 4.3: Band figure for spin-up of Mn$_3$AlC.
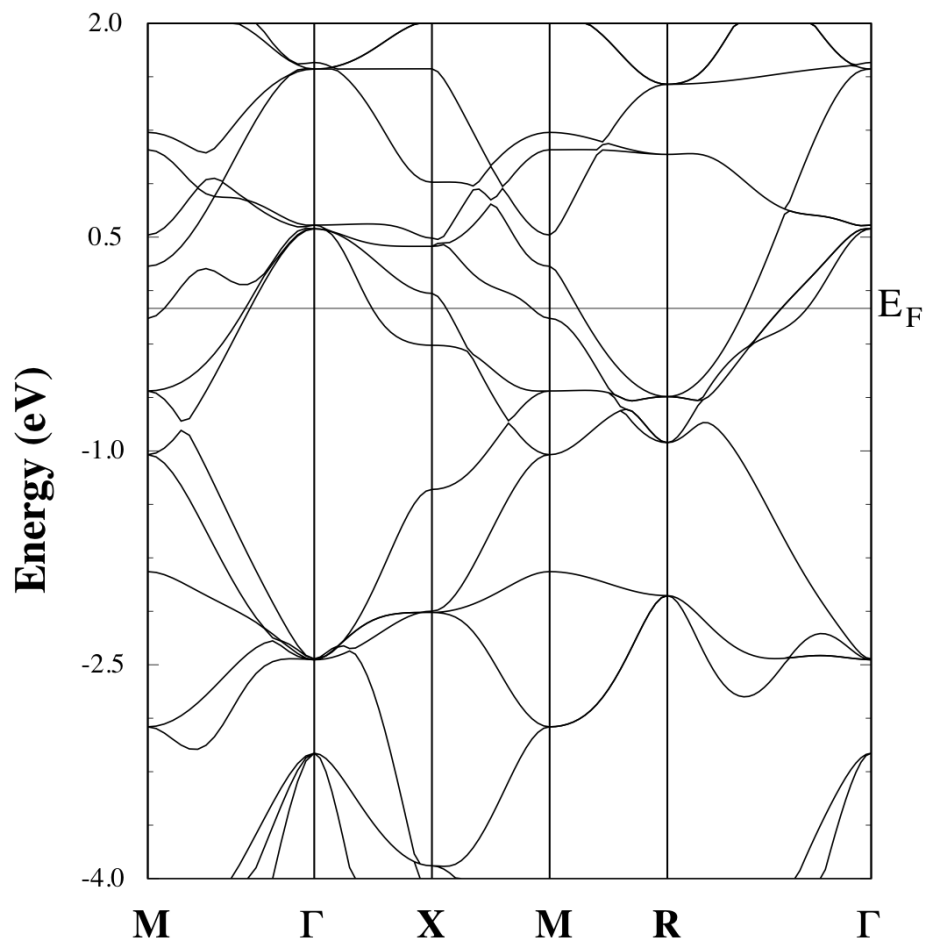
Figure 4.4: Band figure for spin-down of Mn$_3$AlC.
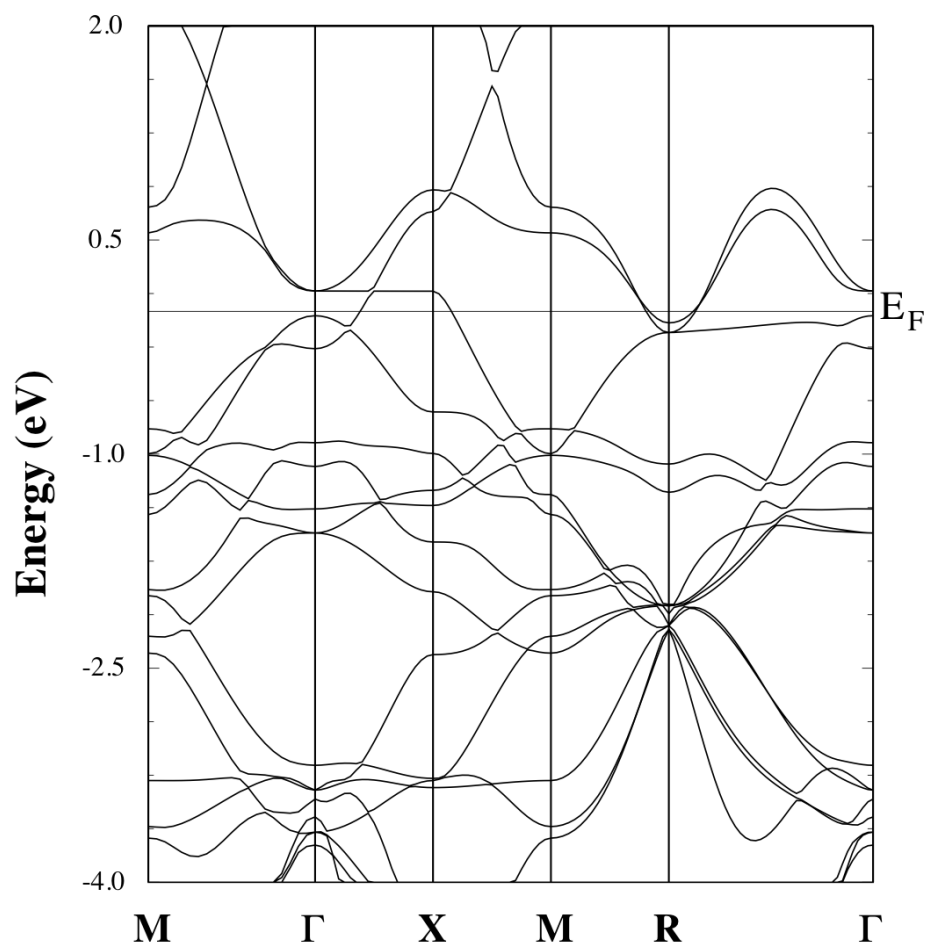
Figure 4.5: Band figure for spin-up of Fe$_2$MnAlC (octa-1).

65
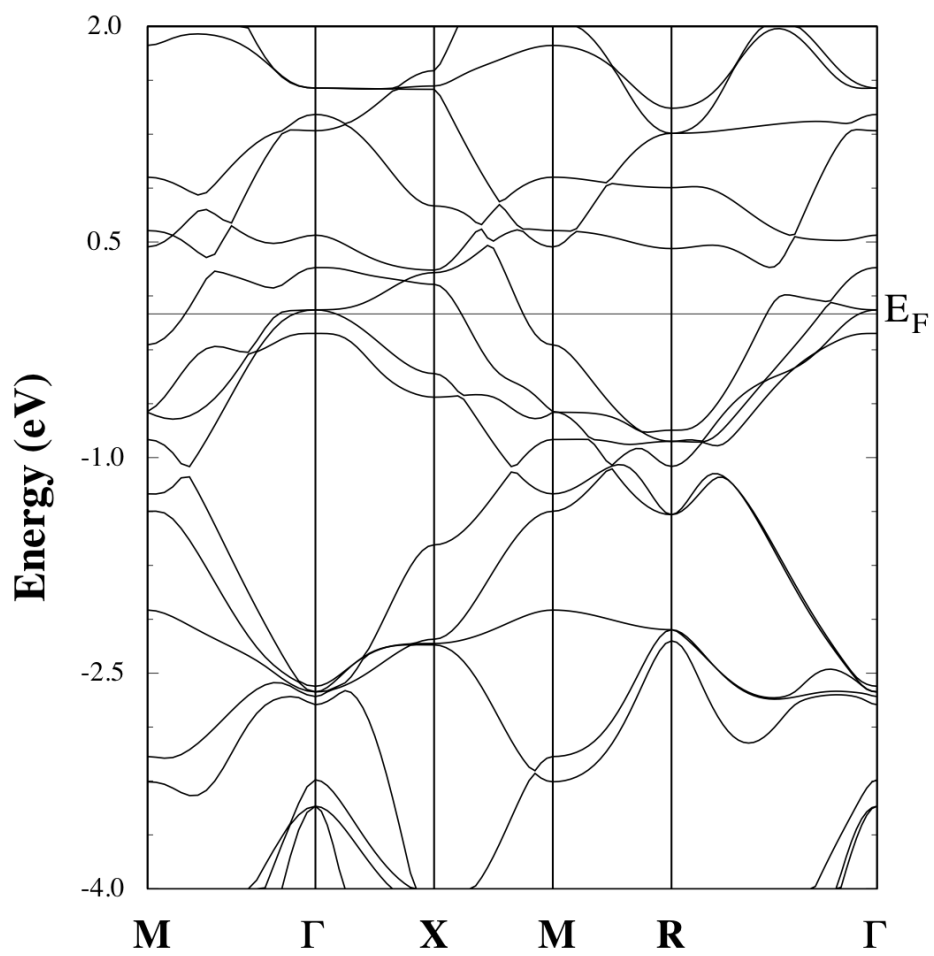
Figure 4.6: Band figure for spin-down of Fe$_2$MnAlC (octa-1).
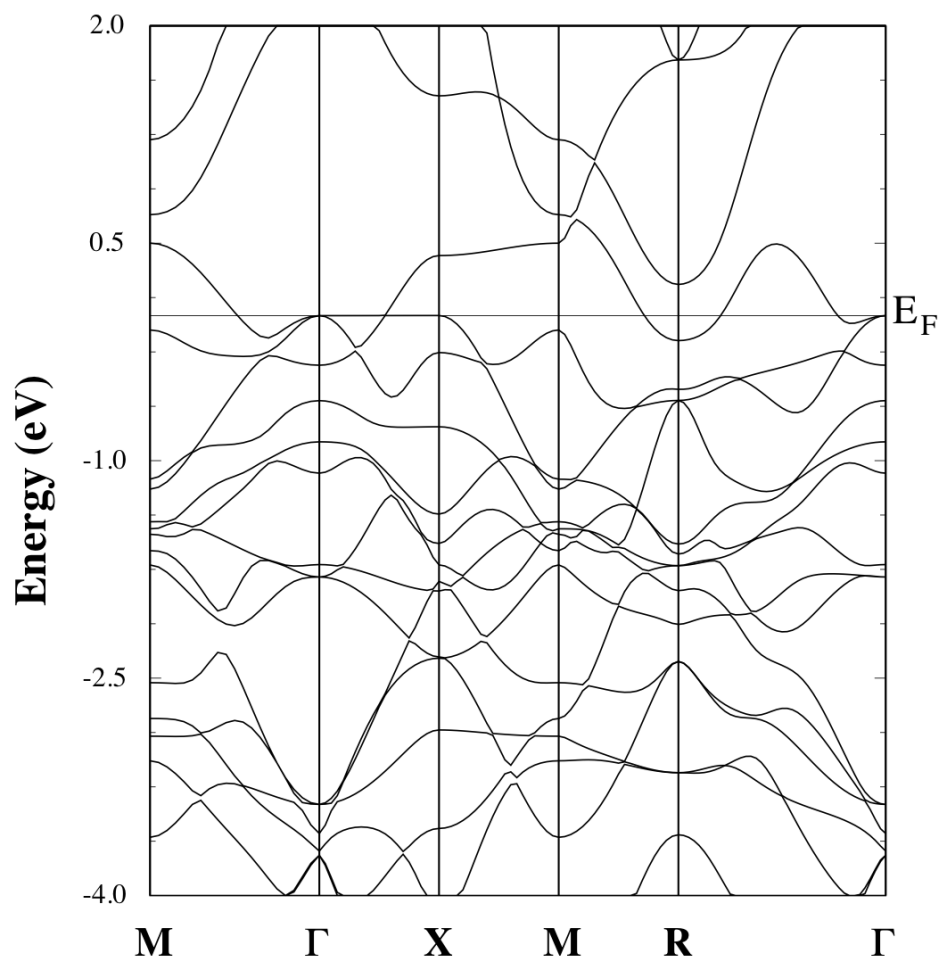
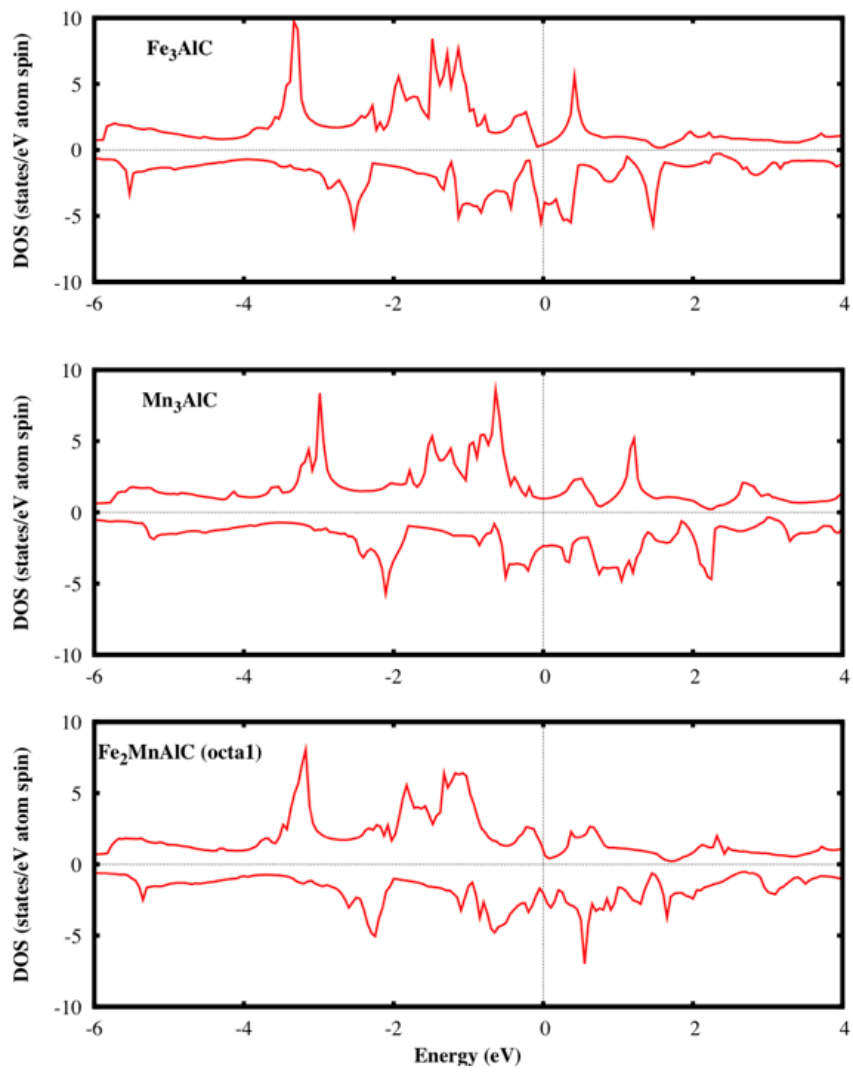Figure 4.7: Band figure of for spin-up Fe$_2$MnAlC (octa-2).
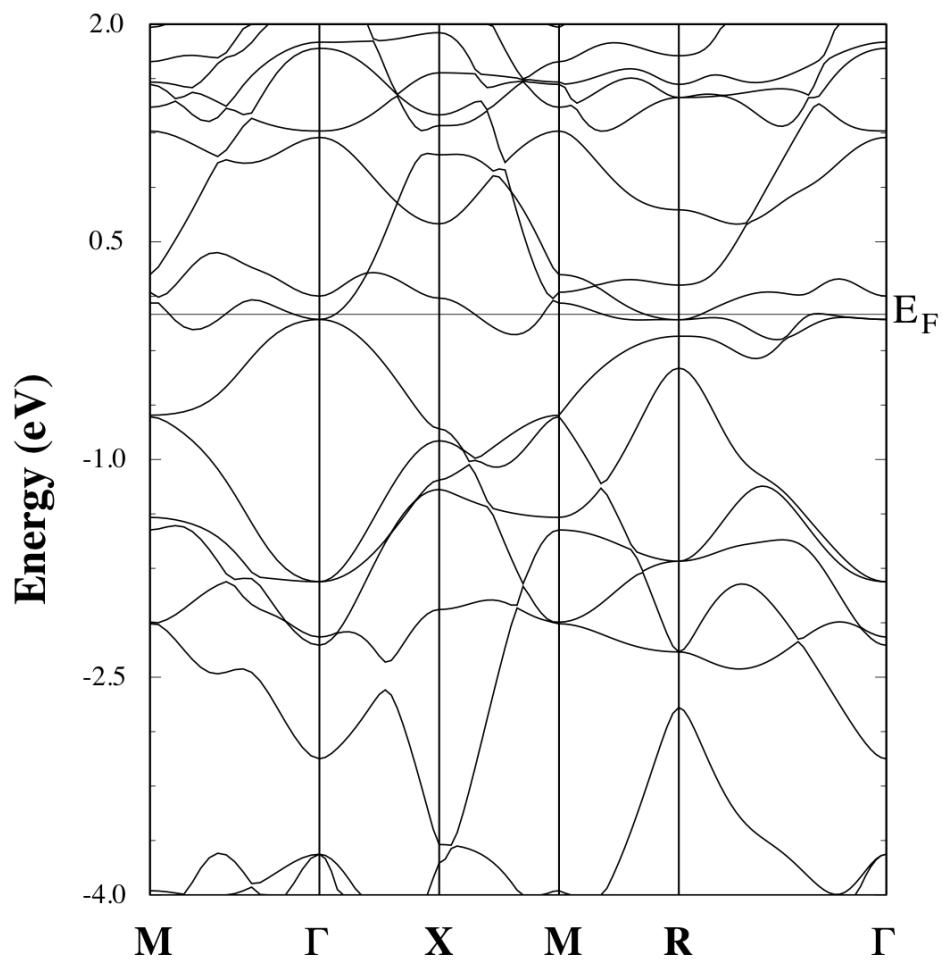
Figure 4.8: Band figure of for spin-down Fe$_2$MnAlC (octa-2).
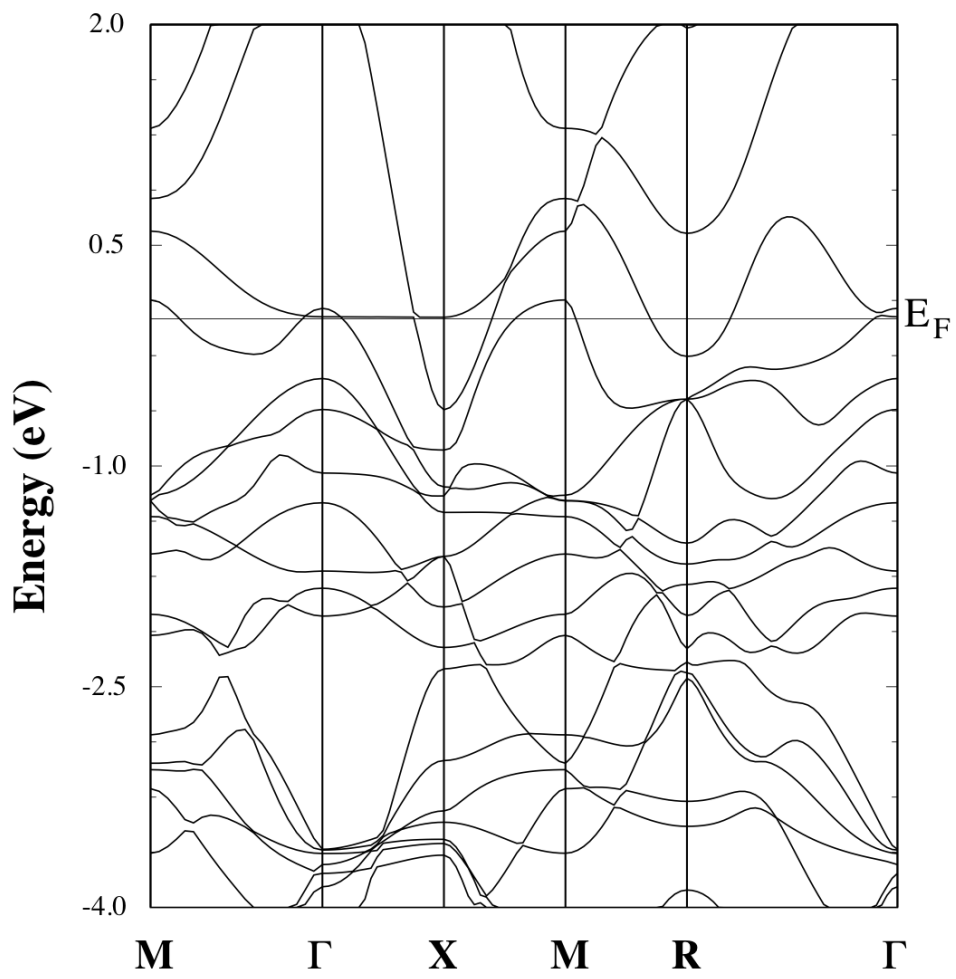
Figure 4.9: Band figure for spin-up of Fe$_2$MnAlC (octa-3).
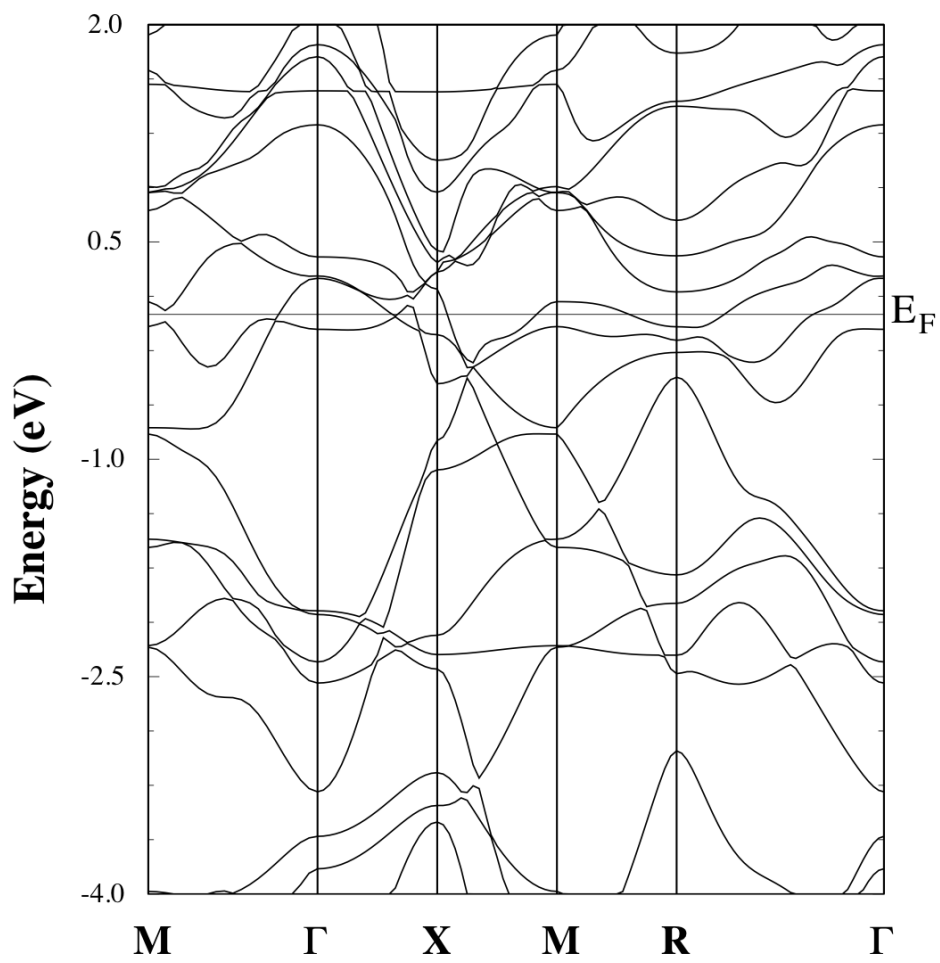
Figure 4.10: Band figure for spin-down of Fe$_2$MnAlC (octa-3).

Figure 4.11: Total density of the states of κ-carbides (to be continue with Fig 4.12).
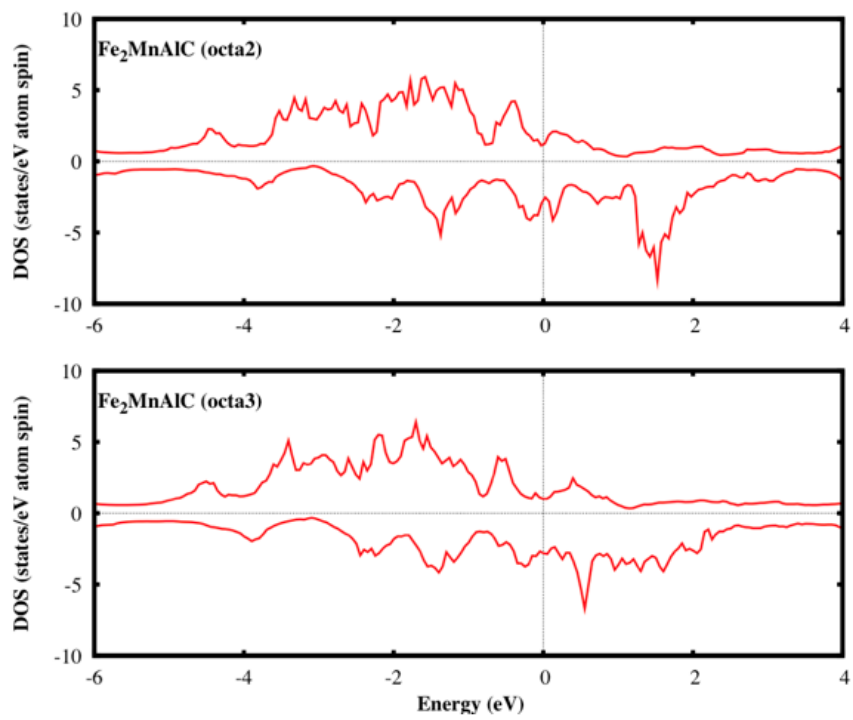
Figure 4.12: Total density of the states of κ-carbides.
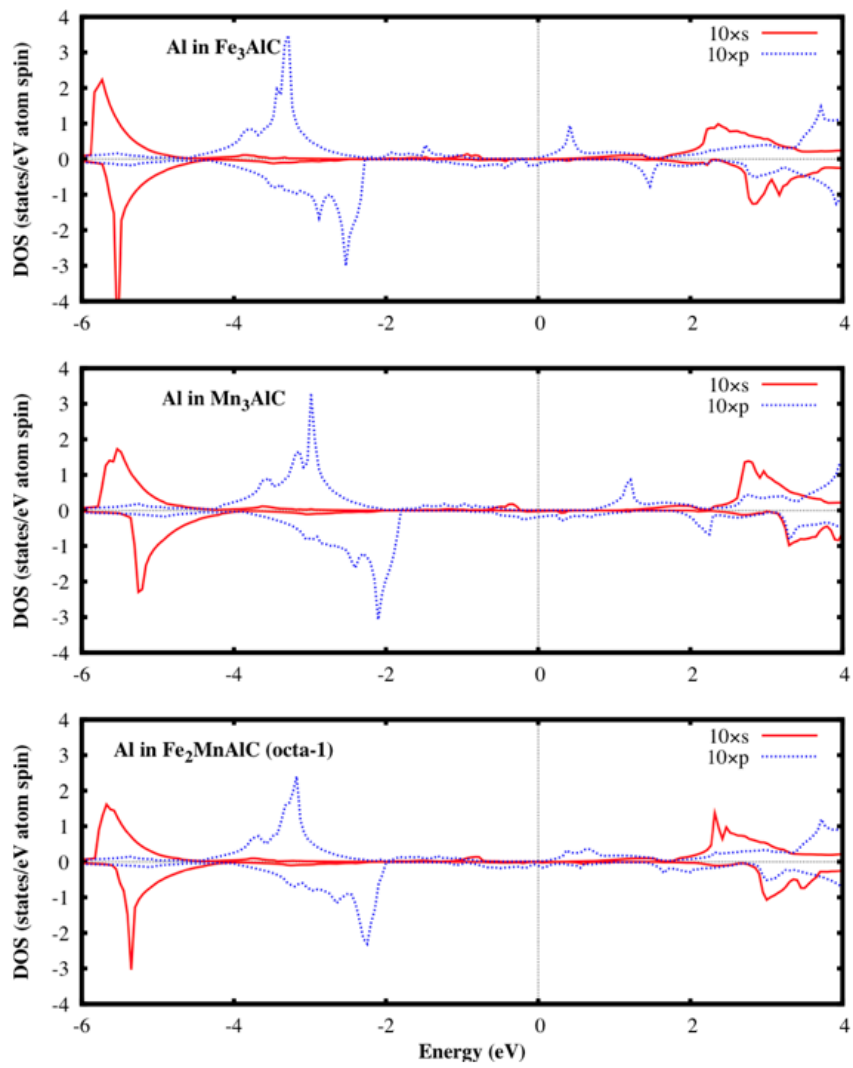
Figure 4.13: Density of the states of Al atom in κ-carbides (to be continue with Fig 4.14).
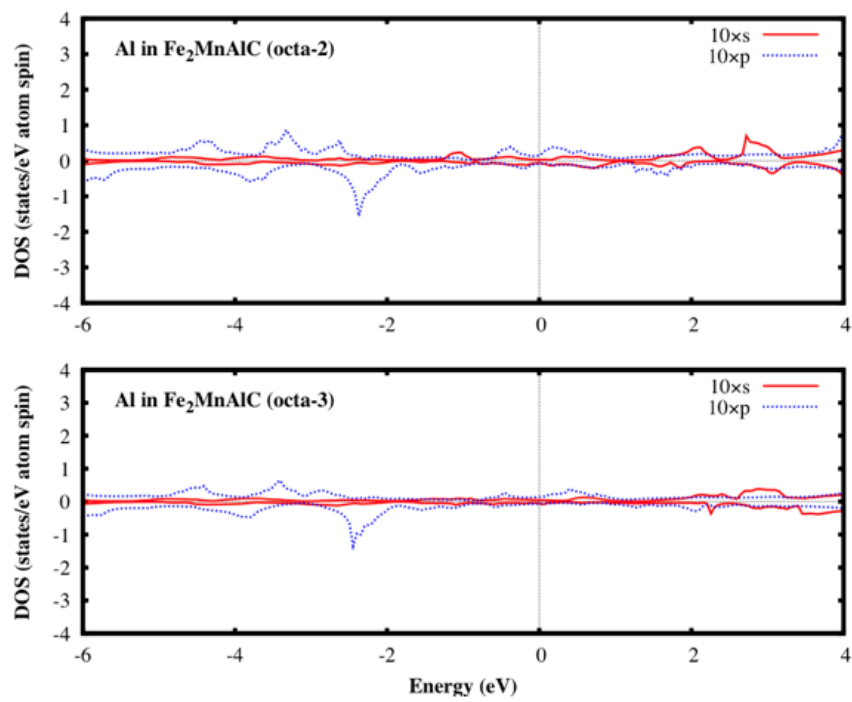
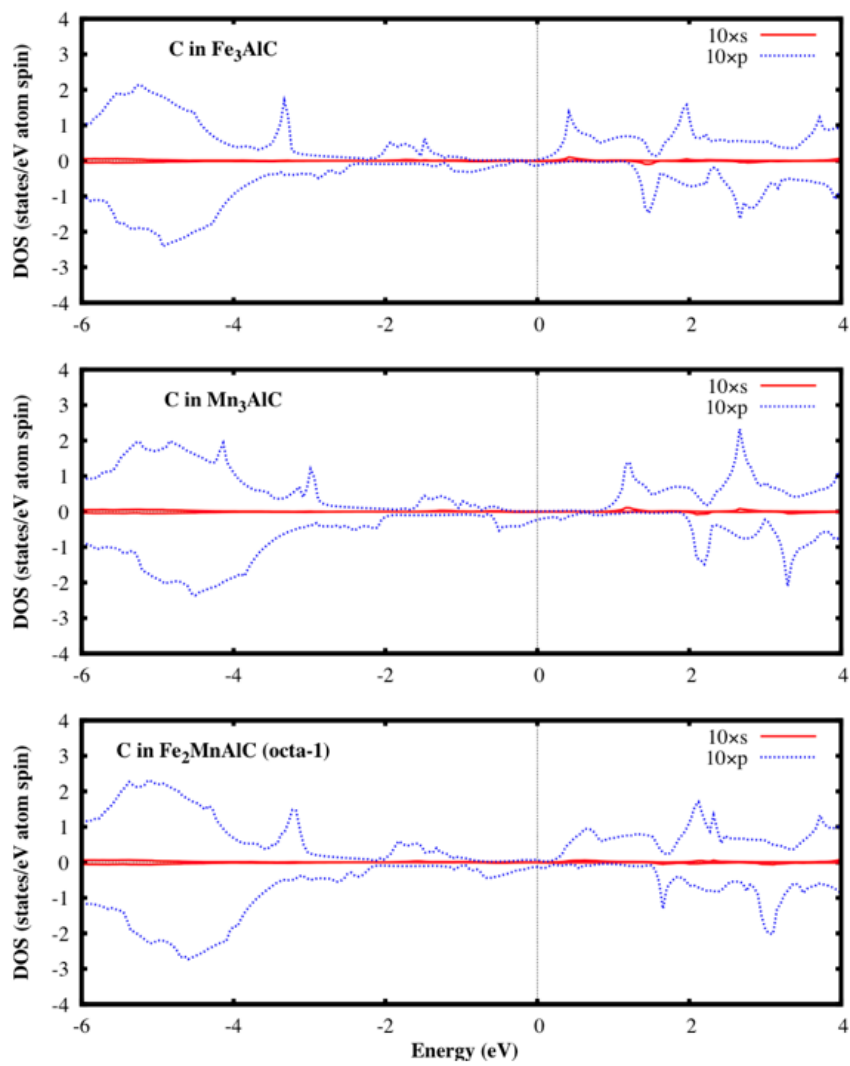Figure 4.14: Density of the states of Al atom in κ-carbides.

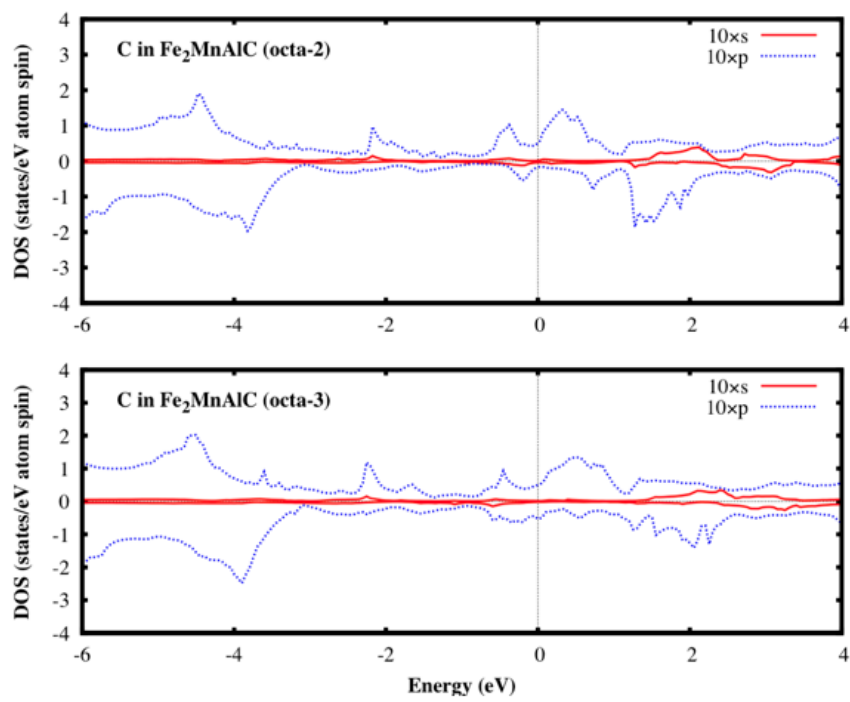Figure 4.15: Density of the states of C atom in κ-carbides (to be continue with Fig 4.16).

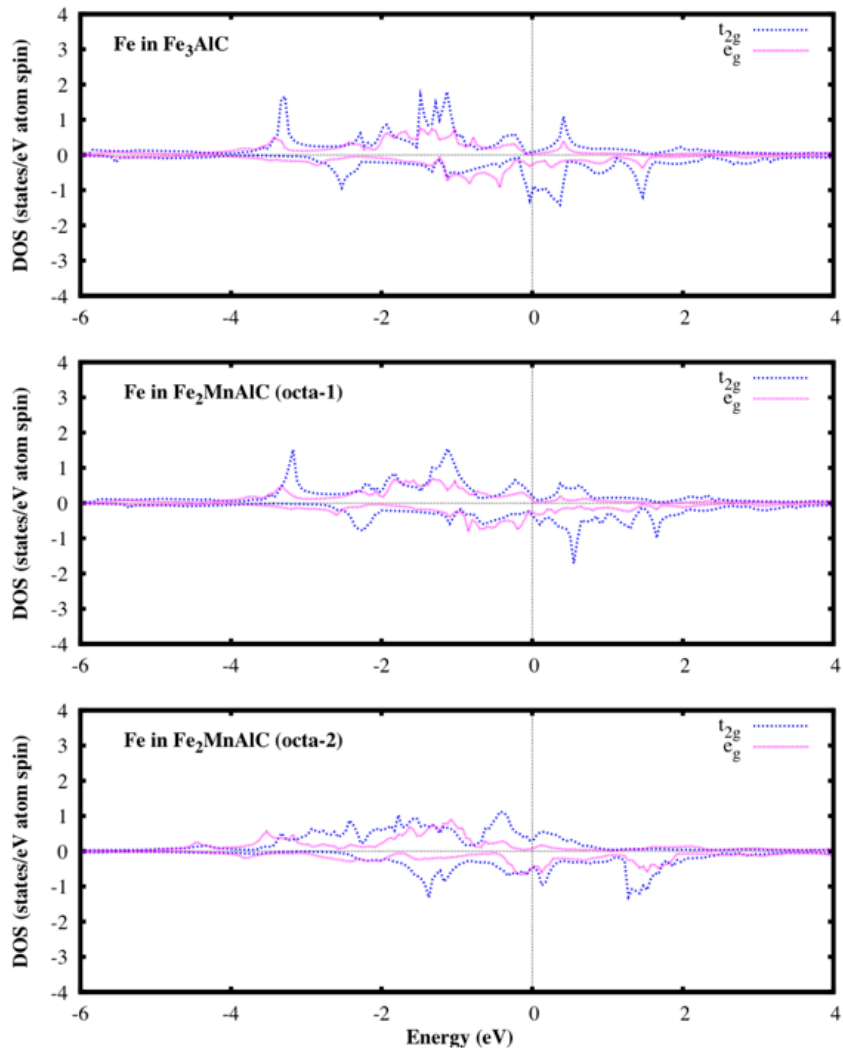Figure 4.16: Density of the states of C atom in κ-carbides.

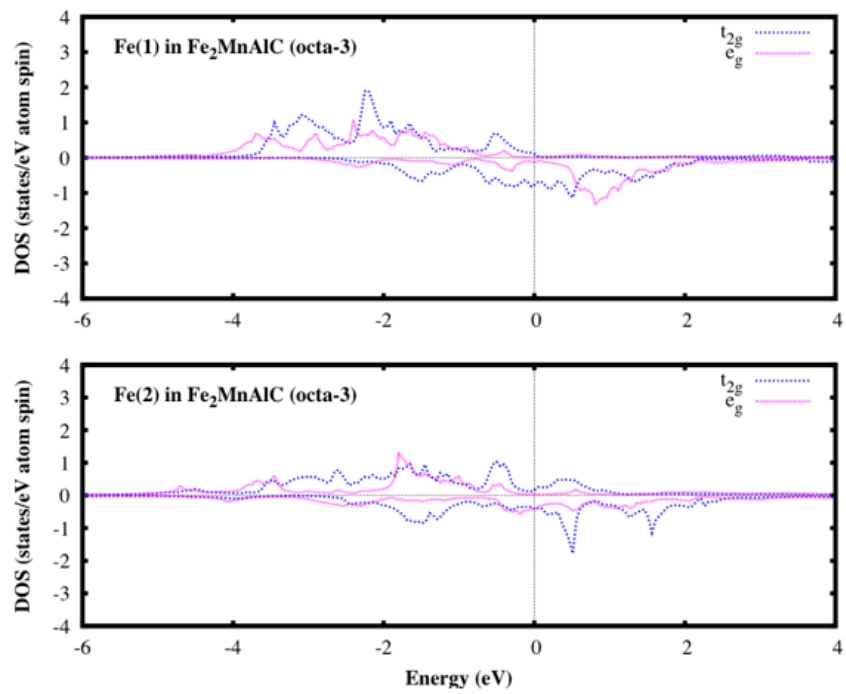Figure 4.17: Density of the states of Fe atom in κ-carbides (to be continue with Fig 4.18).

77

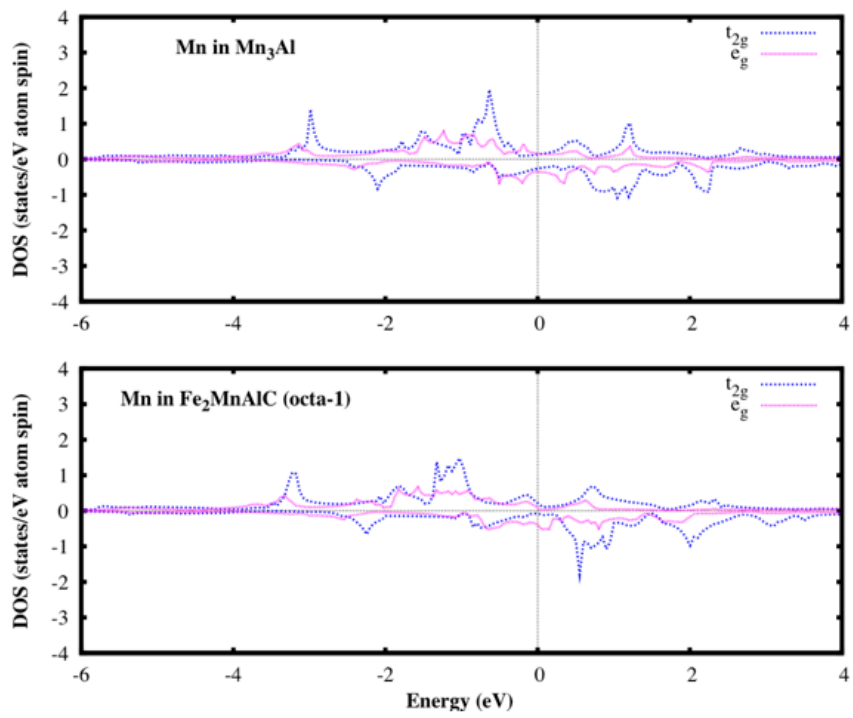Figure 4.18: Density of the states of Fe atom in κ-carbides.

Figure 4.19: Density of the states of Mn atom in κ-carbides (to be continue with Fig 4.20).

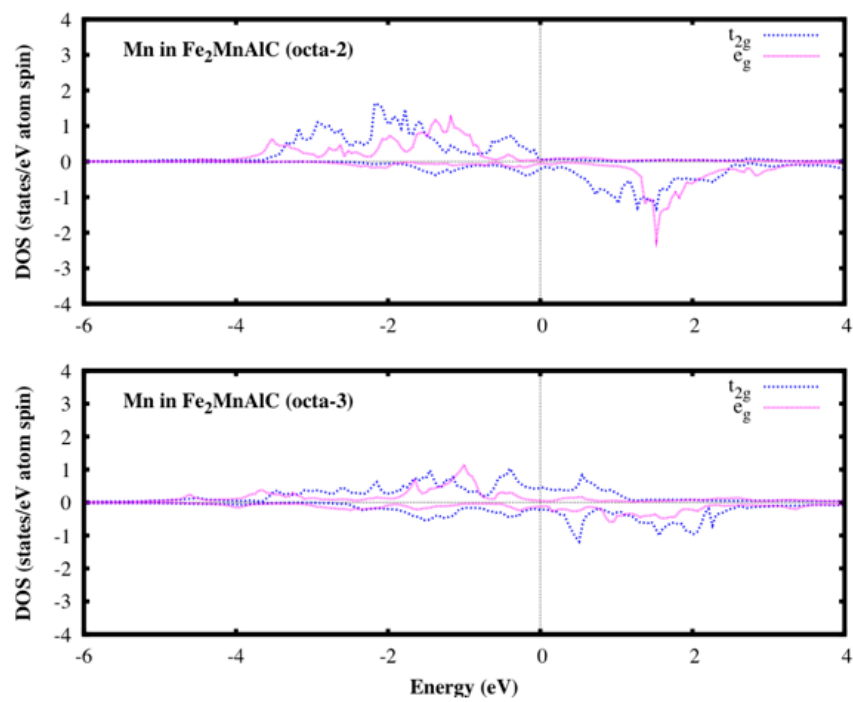Figure 4.20: Density of the states of Mn atom in κ-carbides.

4.5 Monte-Carlo Simulation

In this research, first-principles calculation result was reassessed to finite temperature by using Metropolis and Wang-Landau hybrid Monte-Carlo method. The specific assumptions are summarized in chapter 1.3.

In this calculation, each energies for the states used total energy which was calculated using first-principles calculation. Free energy is calculated from Eq 3.3, Eq 3.10 and Eq 3.11. Also, calculated density of the states $g(E)$ and partition function Z has no dimension and unit of calculated free energy is J. Fig 4.22 shows the result of the Monte-Carlo result. This result shows that there is no phase transition in given temperature range. If there is phase transition, Free energy-temperature graph should change its slope. Fig 4.26 shows the example of the free energy-temperature graph with phase transition. The reason is the cell gas model doesn't include interface energy between each cells and, the temperature range was too high. For example, the Boltzmann constant k_B is 1.381×10^{-23} J/K. so, $0.1\,k_B$T means T $= 7.241 \times 10^{21}$ K and this is why the order of free energy is $\sim 10^{22}$. Also, to validate the Monte-Carlo result, the calculated entropy was compared with configurational entropy that was only considered entropy in this cell gas model. The entropy was calculated from free energy-temperature curve by Eq. 3.8, and from configuration by 3.7.

The free energy-temperature curve was fitted by linear function to calcu-
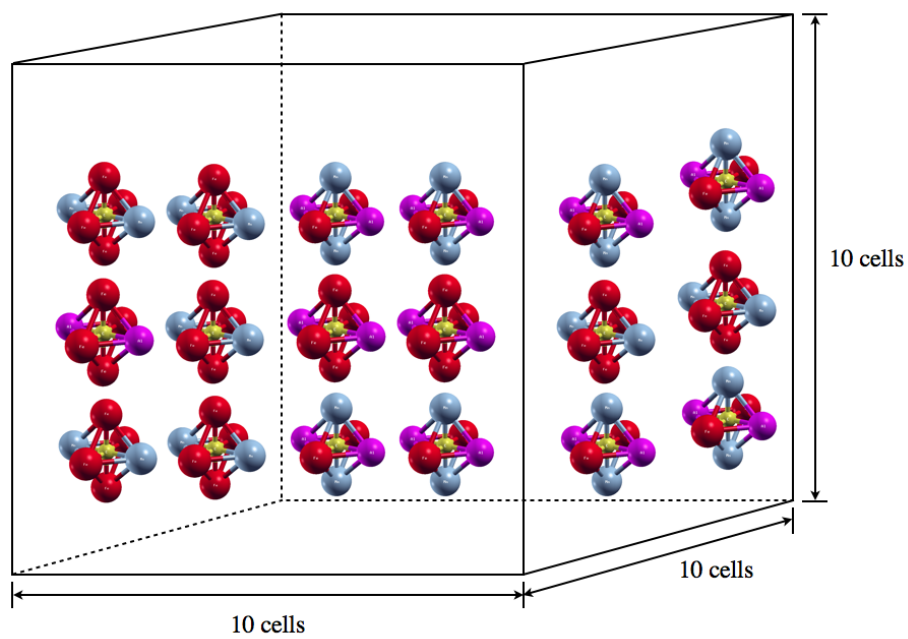
Figure 4.21: Schematic figure of lattice cell gas model. There is cube that has 10^3 unit cells and each cells can change the state freely in between non-magnetic or spin polarized Fe_2MnAlC octa-1 to octa-3.
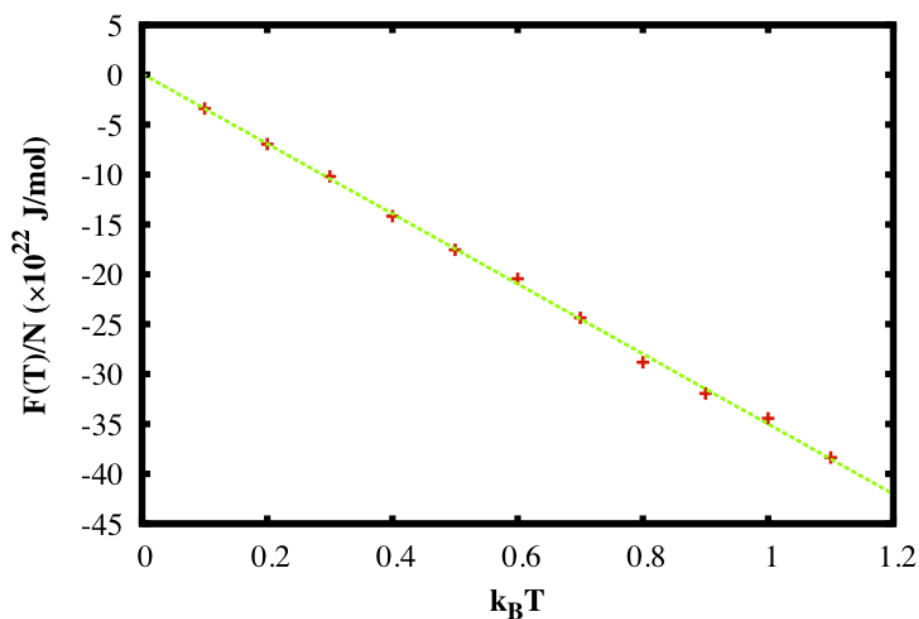
Figure 4.22: Calculated Helmholtz free energy $F(T)$ with respect to temperature. N is the total number of the cell.

late entropy. The entropy from Monte-Carlo result was $4.85 \, \mathrm{JK^{-1}mol^{-1}}$ per cell and all possible configuration with 1000 cells and 6 states for each cell is 6^{1000} so, configurational entropy per cell is $14.90 \, \mathrm{JK^{-1}mol^{-1}}$. Configurational entropy was three times more than calculated entropy. This results might come from implementation problem. The C++ programming language can't deal with number more than 10^{256} however, density of the states sometimes bigger than 10^{256}, so the program in this research reduced
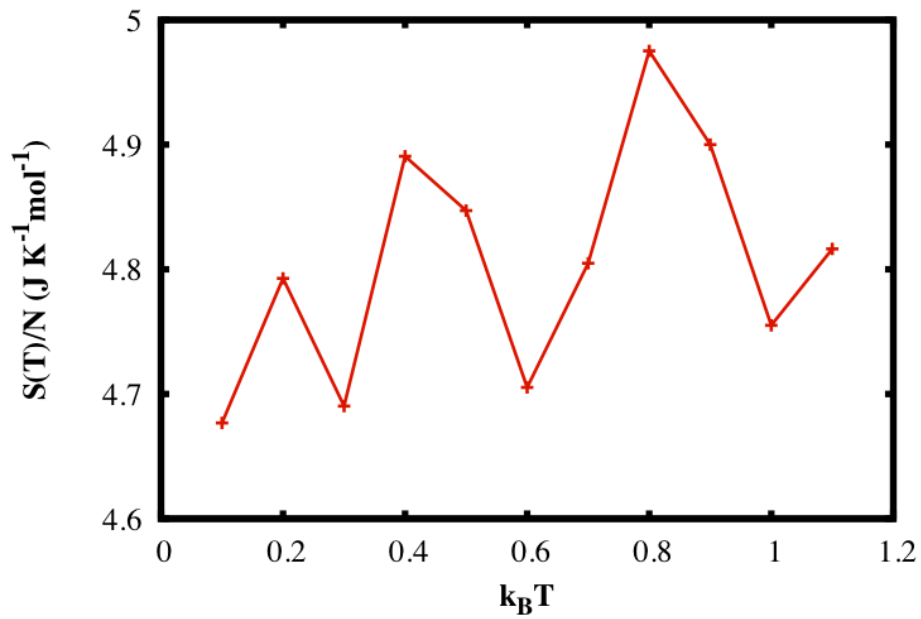
83

Figure 4.23: Calculated entropy $S(T)$ with respect to temperature. N is the total number of the cell.

the system size $(10 \times 10 \times 10)$ and the number of trial visits. Therefore, limited system size and trial visits could not make enough density of the states to calculate exact entropy of the system. By using Eq (3.5), the internal energy of the system can be calculated. According to Eq (3.4), internal energy U should have constant value because the Helmholtz free energy has linear dependence to temperature. The results in Fig 4.24 shows the constant result of calculated internal energy. There is some fluctuations but
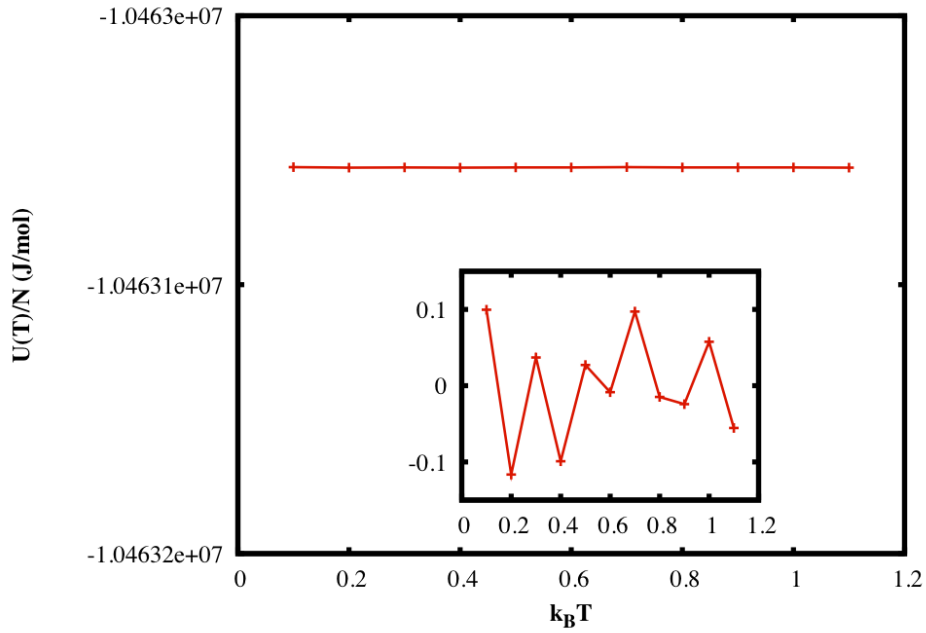
Figure 4.24: Calculated internal energy $U(T)$ with respect to temperature. N is the total number of the cell. The small figure shows magnified internal energy with respect to their average value.

the fluctuation amplitude is very small with respect to internal energy. Fig 4.25 shows the calculated specific heat. The specific heat is also calculated from partition function by following Eq (3.6). Also, it can be calculated from internal energy by

$$C = \frac{\partial U}{\partial T} \tag{4.1}$$

85
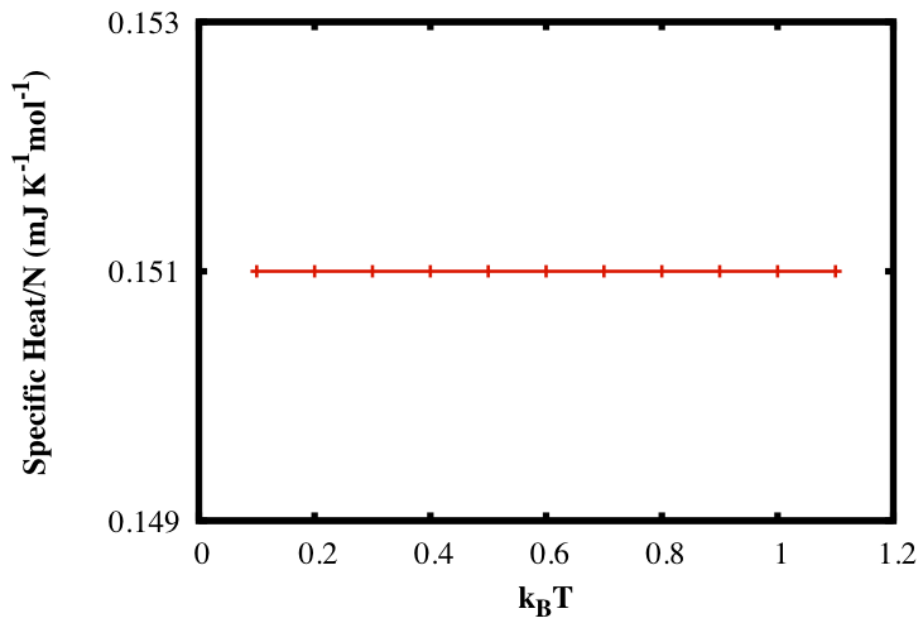
Figure 4.25: Calculated specific heat $C(T)$ with respect to temperature. N is the total number of the cell.

Because U is constant with respect to temperature, the specific heat should have 0. In the result, the specific heat has constant value and that is close to 0. The reason for this results is the fluctuation in free energy, internal energy and entropy.

In summary, even the result of Monte-Carlo simulation didn't expect the exact entropy and the other thermodynamic value, it reflects the general physics of the system well such as tendency and order of free energy, internal

Figure 4.26: Schematic temperature dependence of the free energy and the internal energy for a system undergoing a first order transition (left) and second order transition (right)(Landau and Binder, 2009).
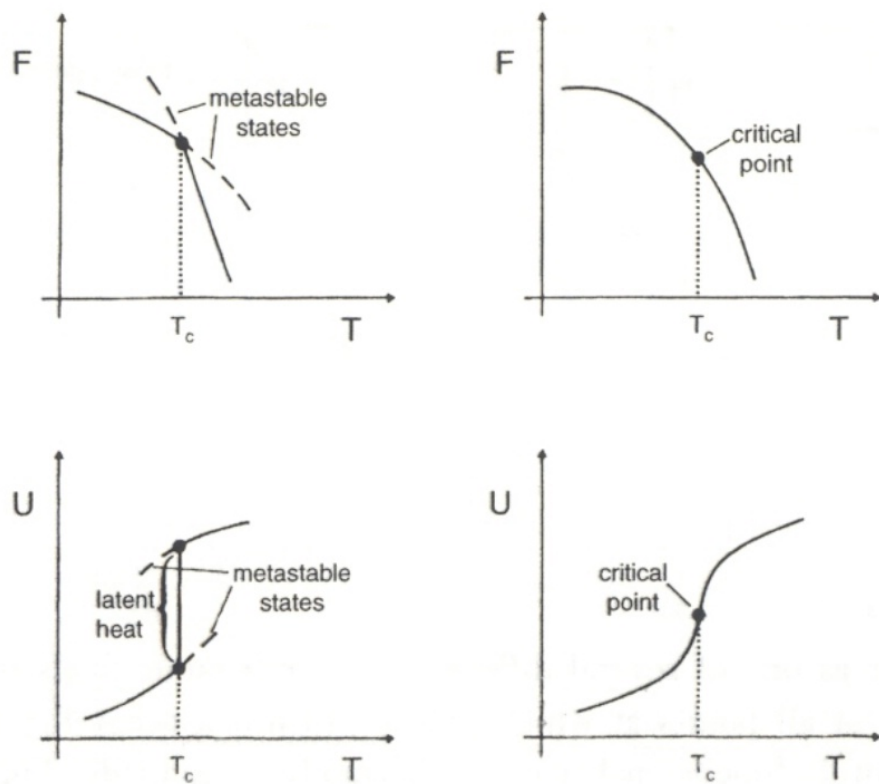
energy, entropy, and specific heat.

5 Conclusion

The structural , magnetic and thermodynamic properties of κ-carbides was investigated using first-principles calculations based on the FLAPW method within GGA. Also, calculated first-principles result was reassessed by using Monte-Carlo simulation. The calculated equilibrium lattice parameter of κ-carbides agrees well with published experimental data.

The calculated formation enthalpies are -16.7 kJ atom-mol^{-1}, -26.2 kJ atom-mol^{-1} and -24.0 kJ atom-mol^{-1} for Fe$_3$AlC, Fe$_2$MnAlC (octa-1) and Mn$_3$AlC, respectively. The calculated formation enthalpies shows that Fe$_2$MnAlC (octa-1) is the most preferred state. Therefore, it is possible that when κ-carbides form, Fe$_2$MnAlC (octa-1) will form first until Mn becomes insufficient in the Fe-Mn-Al-C steels. When the carbon octahedral position was changed, the formation energy becomes positive value and this is explained by p-Al, p-C and d-Fe and d-Mn orbital hybridization breaking in DOS.

The Monte-Carlo cell gas simulation shows the different entropy value with configurational entropy. This result might be caused by implementation problem. However, this simulation well predict temperature dependence of the free energy, internal energy, entropy and specific heat for non-interacting cell gas model.

In the future work, we hope we imply the interaction between cells and the implementation problem will be solved and we can draw the phase diagram of κ-carbides from first-principles calculation and Monte-Carlo simulation by the implementation of the result into thermodynamic database such as MTDATA.

References

Barin, I. (2004). *Thermochemical Data of Pure Substances.* Wiley-VCH Verlag GmbH.

Bhadeshia, H. K. D. H. and Honeycombe, R. W. K. (2006). *Steels: microstructure and properties.* Elsevier.

Blugel, S. (2010). Full-Potential Linearized Augmented Planewave Method.

Burton, B. P., Dupin, N., Fries, S. G., Grimvall, G., Guillermet, A. F., Miodownik, P., Oates, W. A., and Vinograd, V. (2001). Using ab initio calculations in the CALPHAD environment. *Z. Metallkd.*, 92(6):514–525.

Casadei, A. and Broda, R. (2008). Research Report : Impact of Vehicle Weight Reduction on Fuel economy for Various Vehicle Architectures. *The Aluminum Association, Inc.*

Chang, K. M., Chao, C. G., and Liu, T. F. (2010). Excellent combination of strength and ductility in an Fe-9Al-28Mn-1.8C alloy. *Scripta Mater.*, 63(2):162–165.

Chen, C. S., Lin, C. T., Peng, P. W., Huang, M. S., Ou, K. L., Lin, L. H., and Yu, C. H. (2010a). Effects of cobalt content on the microstructures of Fe-9Al-30Mn-1C-xCo alloys. *J. Alloy. Compd.*, 493(1-2):346–351.

Chen, M. S., Cheng, H. C., Huang, C. F., Chao, C.-Y., Ou, K. L., and Yu, C. H. (2010b). Effects of C and Cr content on high-temperature microstructures of Fe-9Al-30Mn-xC-yCr alloys. *Mater. Charact.*, 61(2):206–211.

Chin, K., Lee, H., Kwak, J., Kang, J., and Lee, B. J. (2010). Thermodynamic calculation on the stability of $(Fe, Mn)_3AlC$ carbide in high aluminum steels. *Journal of Alloys and Compounds*.

Choo, W. and Han, K. (1985). Phase constitution and lattice parameter relationships in rapidly solidified $(Fe_{0.65}Mn_0.35)_0.83Al_0.17$-xC and Fe3Al-xC pseudo-binary alloys. *Metallurgical and Materials Transactions A*.

Choo, W., Kim, J., and Yoon, J. (1997). Microstructural change in austenitic Fe-30.0 wt%Mn-7.8 wt%Al-1.3 wt%C initiated by spinodal decomposition and its influence on mechanical properties. *Acta Mater.*

Connetable, D., Lacaze, J., Maugis, P., and Sundeman, B. (2008). A CALPHAD assessment of Al-C-Fe system with the κ carbide modeled as an ordered form of the fcc phase. *Calphad*, 32:361–370.

Connetable, D. and Maugis, P. (2008). First principle calculations of the kappa-Fe3AlC perovskite and iron-aluminium intermetallics. *Intermetallics*, 16(3):345–352.

Franke, P. and Neuschutz, D. (2002). *Thermodynamic properties of inorganic materials.* Landolt-Bornstein. Springer.

Frommeyer, G. and Brüx, U. (2006). Microstructures and mechanical properties of high-strength Fe-Mn-Al-C light-weight TRIPLEX steels. *Steel Res. Int.*, 77(9-10):627–633.

Ghosh, G., van de Walle, A., Asta, M., and Olson, G. B. (2002). Phase stability of the Hf-Nb system: From first-principles to CALPHAD. *Calphad*, 26(4):491–511.

Han, K. and Choo, W. (1989). Phase decomposition of rapidly solidified Fe-Mn-Al-C austenitic alloys. *Metallurgical and Materials Transactions A*.

Han, S. Y., Shin, S. Y., Lee, S., Kim, N. J., Kwak, J. H., and Chin, K. G. (2010). Fracture mechanisms of cold-rolled light-weight steel plates containing different carbon content. *Korean J. Met. Mater.*, 48(5):377–386.

Hobbs, D. and Hafner, J. (2001). Ab initio density functional study of phase stability and noncollinear magnetism in Mn.

Hohenberg, P. and Kohn, W. (1964). Inhomogeneous electron gas. *Phys. Rev*, 136(3B):B864–B871.

Ishida, K., Ohtani, H., Satoh, N., Kalnuma, R., and Nishizawa, T. (1990). Phase-equilibria in Fe-Mn-Al-C alloys. *Isij. Int.*, 30(8):680–686.

Kaufman, L., Turchi, P. E. A., Huang, W. M., and Liu, Z. K. (2001). Thermodynamics of the Cr-Ta-W system by combining the ab initio and CALPHAD methods. *Calphad*, 25(3):419–433.

Kimura, Y., Handa, K., Hayashi, K., and Mishima, Y. (2004). Microstructure control and ductility improvement of the two-phase gamma-Fe/kappa-(Fe, Mn)3AlC alloys in the Fe-Mn-Al-C quaternary system. *Intermetallics*, 12(6):607–617.

Kimura, Y., Hayashi, K., Handa, K., and Mishima, Y. (2002). Microstructural control for strengthening the gamma-Fe/E2(1)-(Fe, Mn)(3)AlCx alloys. *Mat. Sci. Eng. A-Struct.*, 329:680–685.

Koermann, F., Dick, A., Hickel, T., and Neugebauer, J. (2010). Rescaled Monte Carlo approach for magnetic systems: Ab initio thermodynamics of bcc iron. *Phys. Rev. B*, 81(13):134425.

Kohn, W. and Sham, L. (1965). Self-consistent equations including exchange and correlation effects. *Phys. Rev*, 140(4A):A1133–A1138.

Landau, D. P. and Binder, K. (2009). A guide to Monte Carlo simulations in statistical physics. *Cambridge University Press*, page 465.

Landau, D. P., Tsai, S. H., and Exler, M. (2004). A new approach to Monte Carlo simulations in statistical physics: Wang-Landau sampling. *Am J Phys*, 72(10):1294–1302.

Lechermann, F., Fahnle, M., and Sanchez, J. M. (2005). First-principles investigation of the Ni-Fe-Al system. *Intermetallics*, 13(10):1096–1109.

Lee, J., Shishidou, T., and Freeman, A. (2002). Improved triangle method for two-dimensional brillouin zone integrations to determine physical properties. *Phys Rev B*, 66(23):233102.

Liu, Z. K. (2009). First-principles calculations and CALPHAD modeling of thermodynamics. *J. Phase Equilib. Diff.*, 30(5):517–534.

Martin, R. M. (2004). Electronic structure: basic theory and practical methods. *Cambridge University Press*, page 624.

Maugis, P., Lacaze, J., Besson, R., and Morillo, J. (2006). Ab initio calculations of phase stabilities in the Fe-Al-C system and CALPHAD-type assessment of the iron-rich corner. *Metall. Mater. Trans. A*, 37A(12):3397–3401.

Metropolis, N., Rosenbluth, A., Rosenbluth, M., and a. Teller (1953). Equation of state calculations by fast computing machines. *The Journal of Chemical physics.*

Monkhorst, H. and Pack, J. (1976). Special points for Brillouin-zone integrations. *Phys Rev B*, 13(12):5188–5192.

Murnaghan, F. (1937). Finite deformations of an elastic solid. *American Journal of Mathematics*, 59(2):235–260.

Ohtani, H., Yamano, M., and Hasebe, M. (2004). Thermodynamic analysis of the Fe-Al-C ternary system by incorporating ab initio energetic calculations into the CALPHAD approach. *Isij. Int.*, 44(10):1738–1747.

Palatnik, L. S., Tananko, I. A., and Bobro, Y. G. (1964). On the nature of the γphase in the fe-al-c alloys. *Krystallografiya*, 9:209–212.

Palm, M. and Inden, G. (1995). Experimental-determination of phase-equilibria in the Fe-Al-C system. *Intermetallics*, 3(6):443–454.

Pang, L. and Kumar, K. S. (1998). Mechanical behavior of an Fe-40Al-0.6C alloy. *Acta Mater.*, 46(11):4017–4028.

Pang, L. X. and Kumar, K. S. (2000). Tensile ductility of an Fe-40Al-0.6C alloy. *Intermetallics*, 8(5-6):693–698.

Perdew, J., Burke, K., and Wang, Y. (1996). Generalized gradient approximation for the exchange-correlation hole of a many-electron system. *Phys Rev B*, 54(23):16533–16539.

Pollack, H. W. (1988). *Materials science and metallurgy.* Prentice-Hall.

Sato, K., Tagawa, K., and Inoue, Y. (1990). Modulated structure and magnetic properties of age-hardenable Fe-Mn-Al-C alloys. *Metallurgical and Materials Transactions A.*

Seo, S. W., Song, Y. Y., Rahman, G., Kim, I. G., Weinert, M., and Freeman, A. J. (2009). A Convergence Test of the Full-potential Linearized Augmented Plane Wave (FLAPW) Method: Ferromagnetic Bulk BCC Fe. *J. Magn.*, 14(4):137–143.

Tian, X., Li, H., and Zhang, Y. (2008). Effect of Al content on stacking fault energy in austenitic Fe-Mn-Al-C alloys. *J. Mater. Sci.*, 43(18):6214–6222.

Turchi, P. E. A., Abrikosov, I. A., Burton, B., Fries, S. G., Grimvalle, G., Kaufman, L., Korzhavyi, P., Manga, V. R., Ohno, M., Pisch, A., Scott, A., and Zhang, W. (2007). Interface between quantum-mechanical-based approaches, experiments, and CALPHAD methodology. *Calphad*, 31(1):4–27.

Turchi, P. E. A., Drchal, V., Kudrnovsky, J., Colinet, C., Kaufman, L., and Liu, Z. K. (2005). Application of ab initio and CALPHAD thermodynamics to Mo-Ta-W alloys. *Phys. Rev. B*, 71(9):094206.

Wallin, K., Saario, T., and Torronen, K. (1986). Fracture of brittle particles in a ductile matrix. *Int. J. Fracture*, 32(3):201–209.

Wang, F. G. and Landau, D. P. (2001a). Determining the density of states for classical statistical models: A random walk algorithm to produce a flat histogram. *Phys Rev E*, 64(5):056101.

Wang, F. G. and Landau, D. P. (2001b). Efficient, multiple-range random walk algorithm to calculate the density of states. *Phys Rev Lett*, 86(10):2050–2053.

Wang, Y., Curtarolo, S., Jiang, C., Arroyave, R., Wang, T., Ceder, G., Chen, L. Q., and Liu, Z. K. (2004). Ab initio lattice stability in comparison with CALPHAD lattice stability. *Calphad*, 28(1):79–90.

Weinert, M., Wimmer, E., and Freeman, A. (1982). Total-energy all-electron density functional method for bulk solids and surfaces. *Phys Rev B*, 26(8):4571–4578.

Wimmer, E., Krakauer, H., Weinert, M., and Freeman, A. J. (1981). Full-potential self-consistent linearized-augmented-plane-wave method for calculating the electronic-structure of molecules and surfaces - O2 molecule. *Phys. Rev. B.*, 24(2):864–875.

Zhong, Y., Wolverton, C., Chang, Y. A., and Liu, Z. K. (2004). A com-

bined CALPHAD/first-principles remodeling of the thermodynamics of Al-Sr: unsuspected ground state energies by "rounding up the (un)usual suspects". *Acta Mater.*, 52(9):2739–2754.

Curriculum Vitae

Name: Seung-Woo Seo

E-mail: fallen32@postech.ac.kr

Date of birth: 28th April, 1986

Place of birth: Seoul, South Korea

Education

M. S. 2011, POSTECH (Pohang, Korea), Graduate Institute of Ferrous Technology, Computational Metallurgy Group

B. S. 2009, POSTECH (Pohang, Korea), Department of Physics